Energy Conversion and Management: X 29 (2026) 101463

Contents lists available at ScienceDirect

Energy Conversion and Management: X

journal homepage: www.sciencedirect.com/journal/energy-conversion-and-management-x

Comparative analysis of direct-drive and gearbox-coupled electro-hydraulic energy converters

Thomas Heeger [a,*], Martin West [b], Liselott Ericson [a]

[a] Linköping University, Department of Management and Engineering, Division of Fluid and Mechatronic Systems, Campus Valla, Linköping, 58183, Östergötland, Sweden
[b] Tin Arm Engineering, Gothenburg, 41265, Västra Götaland, Sweden

ARTICLE INFO

Keywords:
Compactness
e-pump
Electro-hydraulic energy converter
Fluid power
Gearbox
Off-highway
Permanent-magnet synchronous machine (PMSM)

ABSTRACT

Combinations of electric and hydraulic machines, also known as e-pumps or electro-hydraulic energy converters, are essential for the electrification of mobile working machinery. Currently, these machines are typically combined by axial stacking, and the electric machine directly drives the hydraulic machine. Alternatively, the hydraulic machine can be radially integrated within the core of the electric machine, or a gearbox in combination with a downsized electric machine can be used. However, to the authors' knowledge, no systematic comparison of these different concepts has been published.

This paper uses analytical methods to determine the dimensions of the active parts of hydraulic machines, electric machines, and gearboxes in order to compare different design concepts based on volume, aspect ratio, total mass, copper mass, magnet mass, electromagnetic efficiency, and inertia.

Axially stacked concepts can yield the highest compactness. However, they achieve this compactness at low aspect ratios, with their lengths being several times greater than their outer diameters. For balanced aspect ratios, where the outer diameter and total length of the machine are similar, the radially integrated, direct-driven concept is most compact.

1. Introduction

Mobile working machinery such as excavators and wheel loaders typically use fluid power to drive their motion systems. Positive properties of fluid power systems include excellent power density, robustness, load-holding capabilities, low investment cost, ease of linear actuation, ease of power distribution, shock absorption and overload protection [1]. However, a drawback of conventional fluid power systems is their poor system efficiency, which was estimated to be around 21% for the USA in 2012 [2] and 30% in 2017 [3]. Despite typical component peak efficiencies above 90% [4], the design and operation of fluid power systems typically favour low investment cost, high productivity, and robustness over a high system efficiency. But the reduction of greenhouse gas emissions and rising energy cost require more efficient systems. Many solutions for more efficient fluid power systems are being researched, including energy recovery and the reduction of throttling losses [5]. Electrification is a major part of this trend, and the potential for significant energy savings has been shown (e.g., 62% in the work of Hagen et al. [6], 65% in the work of Qu et al. [7], and 38% to 66% in the work of Hao et al. [8]).

The electrification of hydraulic systems requires not only changes in the system level but also advances on the component level. As a result, research is being conducted on how to best combine electric motors and hydraulic pumps into electro-hydraulic energy converters (also known as e-pumps). Fig. 1 illustrates different concepts for the integration of the machines, with axial stacking or radial integration, and direct drives or gearbox coupling.

Commercially available integrated units are typically axially stacked and direct-driven as sketched in Fig. 1(a) (e.g., [9,10]). Besides modularity and the ease of reusing proven components, axial stacking clearly separates the fluids used in the hydraulic and in the electric machine and allows to install damping blocks between the machines [11]. Alternatively, the idea of a shared housing for the electric motor and a pump for increased compactness was already introduced in 1929 [12]. Later, concepts for even closer radial integration as sketched in Fig. 1(b) were commercialised (e.g., [13,14]). A radial integration of the hydraulic machine within the core of the electric machine is considered to increase compactness (i.e., decrease volume and weight), lower the number of components, eliminate some losses, and reduce external

* Corresponding author.
E-mail address: thomas.heeger@liu.se (T. Heeger).

https://doi.org/10.1016/j.ecmx.2025.101463
Received 28 September 2025; Received in revised form 8 December 2025; Accepted 8 December 2025
Available online 18 December 2025

Table 1
Exemplary collection of statements concerning the compactness of different integration concepts.

Concept	Statement	Source
Direct-driven, axially stacked	Size reductions of 35% to 50% can be achieved by integrating the housings and circulating oil through the electric motor in axially stacked machines.	[19]
Direct-driven, radially integrated	The radially integrated machine requires "up to 50% less space [...] than conventional solutions".	[13]
	The concept "eliminates redundant bearings, seals, and shaft couplings, resulting in lower component cost, reduced mass, and higher power density compared to coupling two separate electric and hydraulic machines".	[20]
	Integrating the housings and rotors of the electric and hydraulic machine "reduces the volume by 40%–50% and the noise by 10 dB-15 dB compared to traditional pumps".	[21]
Gearbox-coupled concepts in general	"Using a gearbox to couple hydraulic machines with power dense electric machines increases the system mass, volume, inertia, and cost".	[20]
Gearbox-coupled, axially stacked	The gravimetric power density of the combined electric machine and gearbox is increased by 15.6% in comparison to a direct-drive electric machine. The volumetric power density is only improved by 1.5%. However, in higher power classes, e.g., 60 kW, an improvement of the volumetric power density by a factor of 2.83 is expected.	[22]
Radially integrated gearbox and axially stacked hydraulic machine	"The electric machine is designed around the planetary gear aiming at a low volume".	[18]

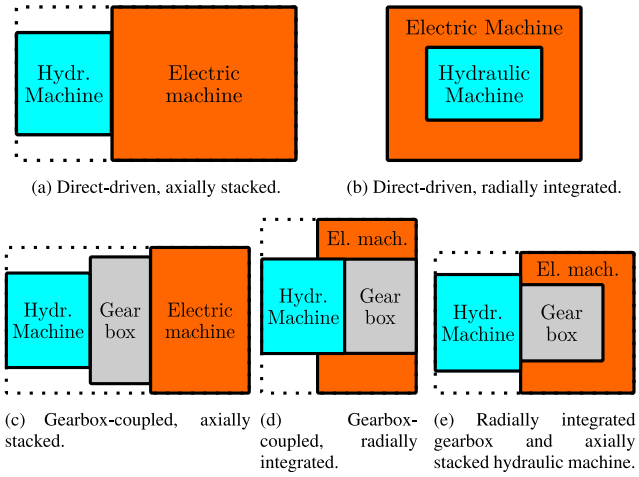

(a) Direct-driven, axially stacked. (b) Direct-driven, radially integrated. (c) Gearbox-coupled, axially stacked. (d) Gearbox-coupled, radially integrated. (e) Radially integrated gearbox and axially stacked hydraulic machine.

Fig. 1. Concepts for combining hydraulic machines and electric machines into electro-hydraulic energy converters.

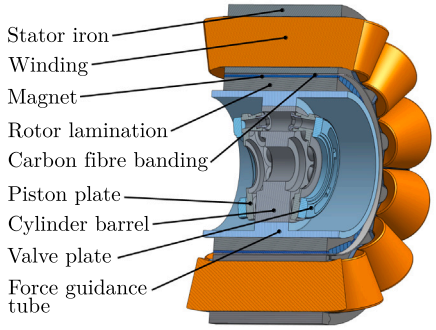

Fig. 2. Sketch of a radially integrated electro-hydraulic energy converter with a hydraulic machine within the core of an electric machine of PMSM type [23]. Note that housing, bearing, and hydraulic channels are not shown in this sketch.

leakage [15]. As a result, this concept has recently attracted growing research interest. Fig. 2 illustrates an example of such a radially integrated machine.

Further, different gearbox-coupled concepts as sketched in Fig. 1(c) [16], Fig. 1(d) [17], and Fig. 1(e) [18] have been developed.

Table 1 includes an exemplary collection of statements on the compactness of different concepts. Radially integrated machines are claimed to increase compactness, and literature includes contradicting statements concerning whether gearbox-coupling increases or decreases the compactness. Typically, sizing and/or optimisation is performed for a single specific concept and systematic concept comparisons between similarly optimised machines are lacking. Previous work of the authors [23] addressed this research gap by providing a concept comparison between axially stacked and radially integrated direct-driven designs using analytical equations. This paper aims to refine the previous work by

- providing an extended literature review.
- considering both hydraulic machines of conventional (single pump) design and hydraulic machines with mirrored rotating groups (double pump design) for each concept, see Fig. 3.
- considering gearbox-coupled concepts. For that purpose, analytical equations for gearbox dimensioning are given.
- extending the method for electric machine dimensioning to accommodate different pole pair and stator slot count combinations, as gearbox-coupled machines run at higher speeds and therefore prefer fewer pole pairs.
- quantifying aspect ratios, material weights, and inertia, in addition to the volume of the active parts and electromagnetic efficiency which were also quantified in previous work.

This paper is structured as follows: Section 2 summarises the literature on different integration concepts for electric and hydraulic machines. Section 3 gives information on the sizing of hydraulic machines of axial piston type, Section 4 summarises the design of permanent magnet synchronous electric machines, and Section 5 describes the design of planetary-type gearboxes. Section 6 compares different concepts on how to integrate the aforementioned machines. Section 7 discusses the results, and adds further considerations for the different concepts. Finally, Section 8 provides conclusions.

2. Literature review

Mobile working machinery such as excavators and wheel loaders typically rely on hydraulics for their motion systems, and often also for their travel systems. In conventional systems, one or more pumps are driven by a combustion engine. The hydraulic power is then distributed to the actuators (cylinders or hydraulic motors) via valves. Those systems typically lack the capability of energy recuperation (e.g., when lowering a load), and suffer from high throttling losses due to the power distribution via valves. Fig. 4 sketches a typical conventional, valve-controlled system setup as well as a decentralised, electrified setup.

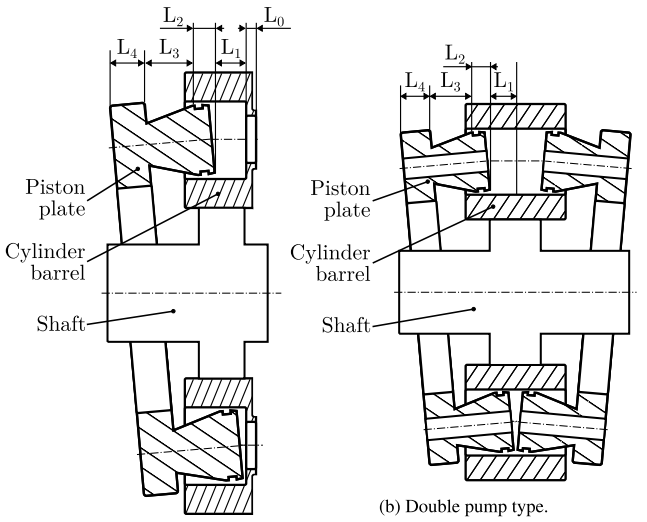

(a) Single pump type.

(b) Double pump type.

Fig. 3. Key lengths of rotating group of an axial piston machine on the example of a floating piston machine [23]. Note that components such as bearings and the housing are not shown in the sketches.

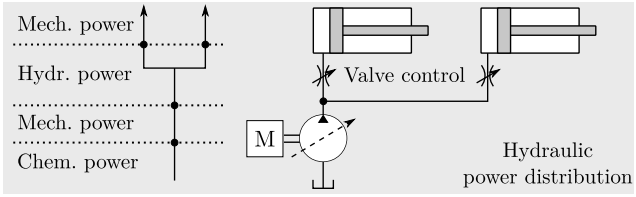

(a) Conventional, valve-controlled system (typically driven by a combustion engine).

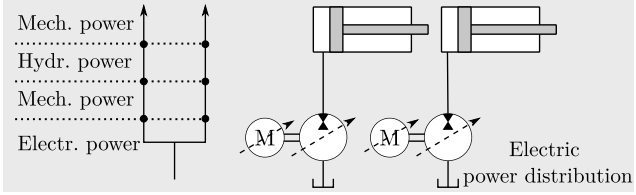

(b) Decentralised system driven by electric motors.

Fig. 4. Concepts for power distribution in mobile working machinery [1].

Electrifying and redesigning the hydraulic systems has the potential for substantial efficiency improvements due to energy recuperation and the reduction of throttling losses, whilst retaining the advantageous properties of hydraulics.

Original equipment manufacturers are expanding their portfolios of electrified machinery, and suppliers are offering dedicated combinations of electric motors and hydraulic pumps (e.g., [9,24]). Typically, these combinations are axially stacked, with shafts directly connecting the two machines. Parker [9] markets this concept for various types of hydraulic machines, in combination with PMSMs.

Compactness is a crucial characteristic for mobile machinery, and decentralised systems may require more installed power. Therefore research is ongoing to increase the compactness of the combined hydraulic and electric machines (hereafter referred to as *electro-hydraulic energy converters*).

2.1. Radial integration of direct-driven machines

One concept is to place the hydraulic machine within the core of the electric machine, leveraging the generally high torque density of hydraulic machines [25] as sketched in Fig. 1(b). Companies and research institutions have investigated this concept for various combinations of electric and hydraulic machines, and an overview of the explored combinations can be found in [15].

The concept was commercialised by Voith Turbo, who claimed space savings of up to 50% for an internal gear machine radially integrated into an asynchronous machine [13], but the product was later withdrawn from the market. RAPA Automotive GmbH & Co. KG started serial production of an internal gear pump radially integrated into a permanent magnet synchronous machine (PMSM) in 2018 [14] (see Section 2.1.5).

Patents and patent applications often cover a wide range of hydraulic and electric machines. Several recent patents and patent applications have focused on cooling, e.g., by using the hydraulic machine's leakage oil [26], by using oil from the hydraulic machine's inlet [27], or by sharing cooling channels between the different components [28,29]. An axial integration of the inverter onto a radially integrated combination of electric and hydraulic machine was also considered [28,29]. The use of a radially integrated electro-hydraulic energy converter in a tightly integrated electro-hydraulic actuator has been suggested [30].

Recent academic publications focusing on integrating permanent magnet machines with different hydraulic machines are summarised below.

2.1.1. Axial piston machines

The radial integration of axial piston machines within PMSMs has attracted multiple research groups.

At Linköping University, previous work by the authors of this paper investigated the radial integration of an axial piston machine of floating piston type within a PMSM [23]. A methodology for analytical predimensioning of integrated machines was presented. The most compact hydraulic machine was selected based on scaling laws (see Section 3), and a 12-slot/10-pole PMSM was designed around it using analytical equations (see Section 4). The compactness of integrating the hydraulic machine inside the PMSM was compared to axially stacking the same machines. Additionally, other aspects such as efficiency, cooling, flooding the airgap, and churning losses were discussed [23].

Purdue University investigated the potential to downsize PMSMs which include a radially integrated axial piston pump [31–33]. For drive cycles where the peak flow and pressure demands did not coincide, field weakening was shown to be applicable to avoid over-sizing the machine and the power electronics [31]. The scope was later expanded to consider the exploitation of the overload capacity and variable displacement, but do not state how overheating is avoided when operation is outside the considered drive cycle, e.g., low speed holding of a high load [32]. Finally, representative drive cycles were considered, and it was concluded that variable pump displacement is mainly advantageous to increase compactness when drive cycles operate at high-pressure low flow conditions, whereas fixed pump displacement is advantageous due to increase efficiencies when operating closer to corner power [33].

Beihang University [21,34–36] integrated an axial piston machine with a brushless DC machine (BLDC). The magnets were mounted directly on the pump's rotor, effectively combining the rotors. They developed a simulation model considering the electromagnetic torque and the hydraulic forces. They found that due to unbalanced radial forces, the rotor's radial position is not constant [34]. They developed a thermal model of their machine and let oil circulate through the housing. They concluded that the heat dissipation from the rotor worked better than from the stator, as the rotor was spinning and the stator was stationary [35]. The pump displacement was not explicitly stated, but the flow-speed relationship showed that it was around 4 cc/rev. Their simulations resulted in a peak efficiency of 82% at 7000 rpm, but experimental validation yielded an efficiency of 66.5% at the same operating point [21]. Later, they applied a boost pressure of 3 bar to the inlet to avoid cavitation and measured efficiencies over the whole

operating range, with most efficiencies being in the range of 55 to 75% [36].

Hunan University [37–39] integrated the rotors of the hydraulic and electric machines into one component by placing a Halbach array of permanent magnets on the rotor of an axial piston machine. They stated that the integrated rotor has little effect on the magnetic flux distribution, and they chose the position of the pistons relative to the magnets in order to minimise the torque ripple. Further, they increased the length of the oil-flooded airgap to reduce friction losses [37]. Further, they analysed rotor deflection in integrated machines [38]. Subsequently, they built a 2.5 kW prototype. They chose a large airgap and thick magnets, to achieve a high flux density, but low friction in the flooded airgap. They reported efficiencies of up to 65% [39].

Sheffield University [40] explored the radial integration of an axial piston machine within a BLDC, targeting aircraft applications. The work considered an oil-flooded airgap, and assumed pre-heated oil with a minimum starting temperature of 0 °C. The drag losses in an oil-flooded airgap increased the required inverter rating, and different operating points (temperature, speed) have different optimal airgap lengths. As a result, compromises between different operating conditions resulted in an increased airgap length.

Qingdao University [41–44] integrated an axial piston machine into different types of electric motors. Additionally, a driveshaft provided an interface, so that their machine couples electric, mechanical and hydraulic power. One version uses an induction machine for a simplified assembly in the absence of permanent magnets [41]. However, they also integrated an axial piston machine with a PMSM. They investigated the NVH behaviour by computing harmonic radial forces of the electric motor and a modal analysis of the stator [42]. They also performed loss calculations with focus on the electric machine [43] and the hydraulic machine [44].

2.1.2. Bent-axis machines

Lappeenranta University of Technology [45–49] investigated the integration of bent-axis machines partially enclosed by a PMSM. Their prototype achieved a peak efficiency of 87% [47]. Hydraulic fluid was used as the coolant for the electric motor, with a particular focus on the use of leakage oil. For their exemplary machine, an oil-flooded airgap of 2.7 mm height caused oil drag losses of 2.6% of the nominal power at the rated operating point [45]. They also demonstrated that friction torque increases significantly with decreasing temperatures.

2.1.3. Radial piston machines

A radial integration of axial flux machines in combination with radial piston machines was explored by researchers at the University of Minnesota and the University of Wisconsin-Madison [20,50–52]. In order to maximise power density, they developed a high-speed pump with a speed of 10000 rpm to match the speed capability of the electric motor. Axial flux machines have been chosen due to their high torque density. The researchers used co-optimisation of hydraulic, electromagnetic, and thermal design to quantify trade-offs between power density, efficiency, torque ripple, cost and rotor moment of inertia [20].

The University of Bath [53] presented and tested an additively manufactured radial piston machine integrated with a BLDC machine and a peak power of 1.2 kW. In this design, the radially integrated piston machine contributed additional stack length to the BLDC machine. The work further introduced measuring the housing reaction torque in shaftless designs, enabling separately analyse of different loss mechanisms.

2.1.4. External gear machines

Purdue University developed and tested a prototype of an external gear pump radially integrated into a surface-mounted PMSM [7,54,55]. The external gear machine was selected due to its cost effectiveness. The hydraulic and electric machine were co-optimised by linking their speed and power requirements. Pareto-fronts for required volume and efficiency were simulated. The prototype achieved a peak efficiency of 69% [54]. The prototype was tested on the boom function of a 5-ton skid steer loader, and the system had a peak efficiency of 60% [7].

Earlier work at TU Dresden and University of Applied Sciences Dresden implemented a radial integration of a switched reluctance motor with an external gear pump [56]. This machine utilised the variable reluctance of the gears, and drove the gears directly from a stator, that was split to drive both gears. The gears were redesigned for improved electromagnetic performance. However, the researchers found limitations in the achievable pressures and operating speeds with this concept.

2.1.5. Internal gear machines

Researchers at Purdue University also developed and tested a prototype of an internal gear pump radially integrated into a surface-mounted PMSM with an oil-flooded air gap [57]. Compared to piston pumps, the internal gear pump offered a cost advantage for low- and medium-pressure applications. The work used a genetic algorithm to create Pareto fronts visualising trade-offs between efficiency and power density. A prototype was tested at speeds of up to 6000 rpm. However, the published test results only showed the volumetric efficiency.

RAPA Automotive GmbH & Co. KG [14] developed an internal gear machine radially integrated into a PMSM for chassis systems in the automotive industry, and included a controller in the integration as well. Concepts involving fully flooded motors were discarded, and a glass fibre-reinforced plastic seal was placed in the magnetic airgap.

2.1.6. Vane machines

Wroclaw University integrated a vane pump into a BLDC machine [58–60]. The vane pump was of double-stroke design, resulting in inherently balanced radial pump forces. A 2.5 kW machine with a maximum speed of 3000 rpm was tested under both static and dynamic conditions.

2.1.7. Other hydraulic machine types

Gamez-Montero et al. [61] integrated a gerotor pump into a permanent magnet motor. Leati et al. [62] integrated an oscillatory pump with a biased reluctance motor, and Khamitov et al. [63] integrated an oscillatory pump into a linear electric motor.

2.2. Gearbox-coupled machines

The hydraulic machine has speed limitations as explained in Section 3.1. Thus, downsizing by simply increasing the hydraulic machine's speed is not feasible. However, it is possible to increase the electric machine's speed and downsize it by introducing a gearbox. Nishanth et al. [20] consider this option, but state that it increases system mass, volume, inertia, and cost, although they do not provide details on how this conclusion was reached.

Known work includes axial stacking of the machines, and a radial integration of the gearbox in combination with axial stacking of the hydraulic machine. These works include detailed designs, but they do not quantify a comparison to direct-driven machines.

2.2.1. Axial stacking

RWTH Aachen University [16,22,64] developed an internal gear pump driven by a PMSM via a planetary gear carrier. The machines were axially stacked as sketched in Fig. 1(c), and the target application was a mini excavator. The displacement of the pump was 3.88 cc/rev, and it was operated with up to 10000 rpm [22]. The work included a concept comparison, which demonstrated the increased power density of a high-speed electric motor paired with a gearbox in comparison to an electric motor without a gearbox. A planetary gearbox was chosen due to its high compactness, high efficiency, and coaxial alignment of input and output shafts. For a ratio of 3, and high speeds, a fixed carrier shaft was identified as the most advantageous concept, since it avoids

centrifugal forces, splashing losses and lubrication problems caused by a rotating carrier shaft [16]. Jacobs et al. [22] quantify the reduction of the electric motor volume with increased speed based on available machines on the market, but do not assess the effect on the combined volume of electric motor, gearbox and pump.

2.2.2. Radial integration of the gearbox

Lappeenranta University of Technology [18,65] radially integrated a planetary gearbox into an oil-cooled PMSM, and combined it with a bent axis machine partially embedded within the PMSM's core, and partially stacked onto it. This concept is similar to the sketch in Fig. 1(e), with the added integration of pump bearings into the space inside the PMSM's core as well. An outer-rotor PMSM with 24 slots and 20 poles was chosen. As the gearbox was within the core, the connection between rotor and gearbox required additional axial length. The nominal power of the hydraulic and electric machine were 7 kW. The 'air gap' was flooded with oil, and it was stated that the losses due to this were below 3%. The ring gear was stationary (attached to the stator), the sun gear was driven by the rotor, and the carrier shaft was driving the hydraulic machine. The gear ratio was 3. The system was tested stand-alone as well as on a log loader. Two different cooling approaches were tested [65]: immersive oil cooling, and oil flow cooling.

A radial integration of both the hydraulic machine and the gearbox in an electric machine was also considered by Parker-Hannifin. Their patent also considered the axial integration of the inverter onto the machine [17].

3. Hydraulic machine design

This study focuses on axial piston machines, which are very commonly used in mobile working machines due to their high efficiency, high power density, capability to operate at high pressure levels, and low operating cost [66]. Piston machines also have a higher displacement density than other machine types [25], which is an advantageous property for a compact integration.

3.1. Sizing and compactness

To enable a comparison across different axial piston pump concepts, Achten et al. [67] presented scaling laws for the rotating groups of conventional swash plate-type axial piston pumps and floating cup pumps. Other parts such as housings and bearings were neglected. Previous work by the authors [23] extended this methodology to floating piston pumps. The rotating group is the main driver of the size of a hydraulic machine and is used as a proxy to quantify machine size in this work. The displacement V_{hyd}, i.e., the amount of displaced fluid per revolution, is a core parameter for hydraulic machines as it defines the relationship between speed and theoretical (i.e., loss-free) flow rate (see Eq. (1)), and also is proportional to the theoretical torque of the machine (see Eq. (2)).

$$Q_{\mathrm{th}} = n_{\mathrm{hyd}} \cdot V_{\mathrm{hyd}} \cdot \varepsilon_{\mathrm{hyd}} \tag{1}$$

$$T_{\mathrm{th}} = \frac{\Delta p \cdot V_{\mathrm{hyd}} \cdot \varepsilon_{\mathrm{hyd}}}{2\pi} \tag{2}$$

The scaling laws enable the selection of the most compact machine design for a given displacement, or the calculation of the length of the rotating group for a given displacement and outer diameter. The scaling laws rely on the main dimensions of existing machines to compute dimensions for other machines under consideration of varying load and loadability (e.g., stiffness) for other dimensions. Fig. 3 visualises an example for the lengths of the different parts of the rotating group of a floating piston machine. Note that both conventional (single) pumps as well as double pumps with mirrored rotating groups are considered. For the same displacement, double pumps exhibit greater axial lengths but reduced diameters [23].

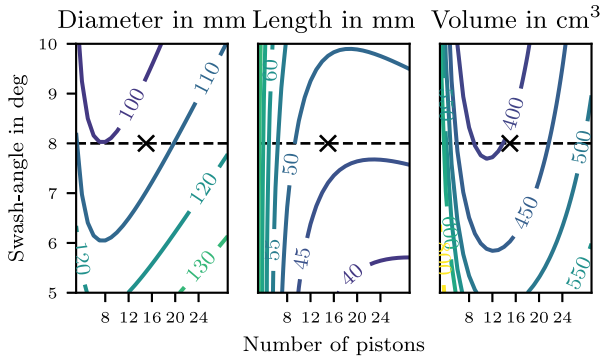

(a) Single pump type.

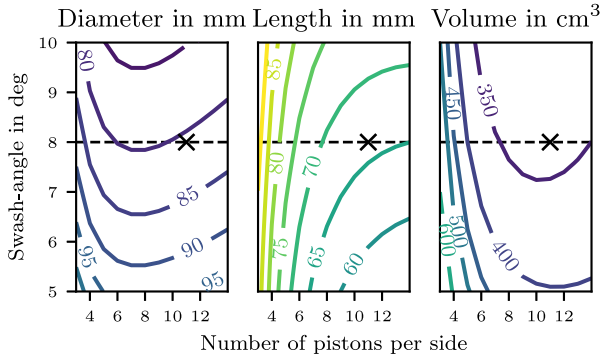

(b) Double pump type.

Fig. 5. Rotating group outer diameter, axial length, and volume for floating piston machines with a displacement of 35 cc/rev. The crosses mark the designs of reference machines [23].

Hydraulic machines are limited in their high-speed capability in comparison to electric machines. Manring et al. [68] formulated scaling laws for the speed limitation due to cylinder block tipping, slipper tipping, and cylinder block filling, and found that all three mechanisms obey the same scaling law in Eq. (3). The scaling law shows increased high-speed capabilities for decreased machine sizes.

$$\frac{n'_{\mathrm{hyd,max}}}{n_{\mathrm{hyd,max}}} \propto \left(\frac{V_{\mathrm{hyd}}}{V'_{\mathrm{hyd}}} \right)^{1/3} \tag{3}$$

3.2. Sizing results

Previous work by the authors [23] compared the compactness of different types of axial piston machines, and concluded that a floating piston pump of the double pump type is the most compact and suitable for the radial integration within an electric machine.

Figs. 5(a) and 5(b) show the outer diameter, axial length, and volume of the rotating group of floating piston machines as a function of the piston count and the swash angle, for a displacement of 35 cc/rev [23]. Note that the maximum displacement angle for floating piston machines is limited to approximately 8° [69]. The figures show that the reference machines are designed very close to the maximum compactness for their displacement angles, but, in principle, different combinations of lengths and diameters can yield the same displacement.

4. Electric machine design

Section 2 showed that PMSMs are the dominant type of electric machine considered for integration with hydraulic machines. Some

advantageous characteristics of PMSMs are their high efficiency, high torque density and fast torque response [70]. The high efficiency also reduces the cooling requirements [57]. The torque requirement on the electric machine and consequently its size can be reduced by leveraging the machine's overload capability in combination with variable displacement of the hydraulic machine. Note that most PMSM use permanent magnets made from rare-earth elements, which the European Union considers as critical materials due to their economic importance and their supply risk [71], and there is concern over the environmental and social impact of rare-earth mining. Therefore, there is a trend to reduce (see [72]) or eliminate (see [73]) the use of rare-earth permanent magnets in electric machines.

The baseline machine in this paper uses surface-mounted magnets, as this increases the rotor's inner diameter and facilitates a radial integration. Yang et al. [74] compared the design and performance between a machine with surface-mounted magnets and a machine with interior-mounted magnets for the same application and traction. They found very similar capabilities for both set-ups, however, with slightly larger stator outer diameters and use of copper material when using surface-mounted magnets. For low torque ripple and simplicity, this paper assumes surface-mounted magnets for all machine setups.

4.1. Sizing of baseline machine (Direct drive)

The torque creation of a PMSM is based on Lorentz force (see Eq. (4)) and a lever arm defined by the rotor's radius.

$$F = B I L_{\mathrm{act}} \tag{4}$$

For rough dimensioning of PMSMs, the electrical loading Q_{rms}, which represents the current per circumference is introduced, see Eq. (5) with the number of turns z_{c}, the current I, and the rotor radius R_{rot}.

$$Q_{\mathrm{rms}} = \frac{z_{\mathrm{c}} I}{2\pi R_{\mathrm{rot}}} \tag{5}$$

Eqs. (4) and (5) can be combined to provide a simple expression for the torque of an electrical machine (see Eq. (6)). Furthermore, the magnetic shear stress in the airgap is introduced in Eq. (7). The magnetic shear stress is the product of the magnetic and electrical loading of the machine, and the torque is proportional to the magnetic shear stress and the volume enclosed by the airgap [75,76]. Typical values of magnetic shear stress for PMSMs are from 40 to 60 kPa, but water-cooled machines can achieve up to 100 kPa [75]. This paper assumes a magnetic shear stress of around 50 kPa. In comparison to the Refs. [75,76], Eq. (6) is extended by the winding factor k_{w} to enable a fair comparison between different machine types. The winding factor summarises the effect of distribution, pitch and skew factors on the available voltage in a phase winding [77].

$$T = B_{\mathrm{rms}} Q_{\mathrm{rms}} 2\pi R_{\mathrm{rot}}^2 L_{\mathrm{act}} k_{\mathrm{w}} \tag{6}$$

$$\sigma = B_{\mathrm{rms}} Q_{\mathrm{rms}} \tag{7}$$

Fig. 6 shows an analytical procedure for the pre-dimensioning of a surface-mounted PMSM. The methodology is based on a previous publication [23] and the reader is referred to this publication for more background. This paper adds more detail to the analytical method to enable a fair comparison between different machine configurations (slot count and pole count). For each machine configuration, its specific winding and fill factors are taken into account.

The magnets are designed to provide the desired magnetic flux in the airgap. The stator teeth and back iron are designed to guide this flux. The maximum magnetic flux density for stator teeth is typically chosen in the range of 1.7 to 1.8 T [75]. For each machine type, the relationship between the slot arc and the magnet arc affects the stator flux density and therefore the required stator teeth and yoke thicknesses. Furthermore, it affects the estimation of the root mean square flux density, which is used for analytical computation of the iron losses.

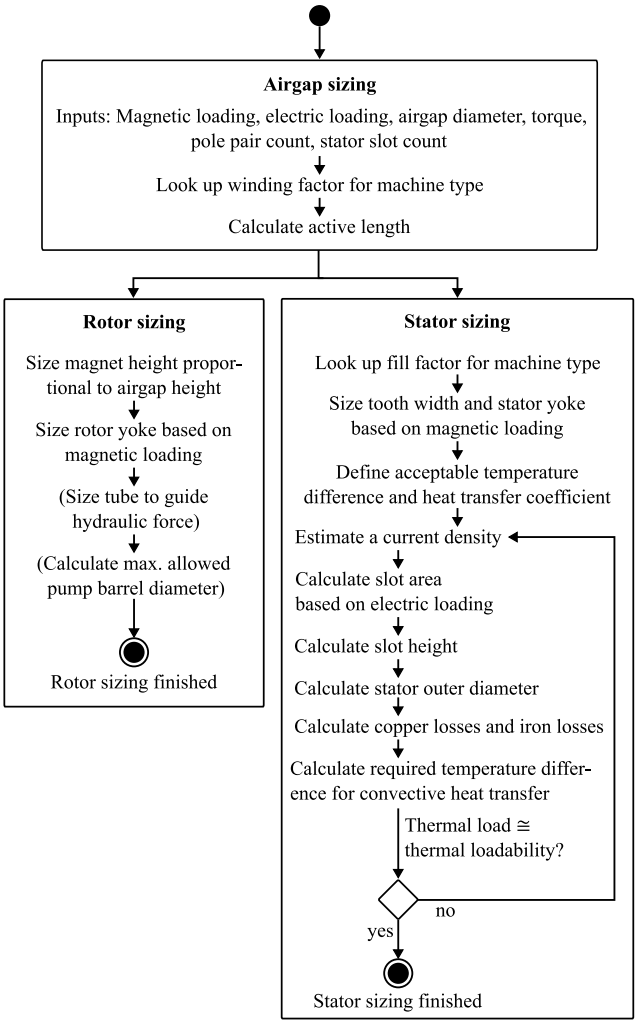

Fig. 6. Procedure for dimensioning of electric machine, modified from [23].

The stator design must consider both the magnetic and the electric loading. The stator slot area in combination with the fill factor and the current density determines the electric loading. The magnetic loading is limited by the magnetic material and the dimensions of the magnets. The electric loading is mainly limited by the machine's cooling capacity. This also implies that a higher cooling capacity allows for more compact machines at the expense of decreased efficiency. Both magnetic and electric loading are not trivial to increase for a given machine type.

The sizing of electric machines aims to avoid overheating. This work considers the stator iron and copper losses, and neglects the losses in the rotor. For continuous operation, the machine's losses must not exceed the cooling capacity at the specified maximum temperature. For this reason, the applied cooling technology (e.g., air cooling, liquid cooling) strongly affects the machine's size. Forced convection using liquids offers a broad range of heat transfer coefficients from 50 to 20 000 W/m^2/K [78]. The relative heat convection coefficient is 43 for water compared to air, and 5 for cooling oil [75], and the heat capacity of water ($4.27 \cdot 10^6$ J/(m^{3}K)) is higher than for oil ($1.8 \cdot 10^6$ J/(m^{3}K)) [79], making water cooling more effective than oil cooling. Additionally, water requires lower circulation pressures than oil [75].

Applications with highly dynamic drive cycles such as mobile working machinery can exploit the PMSM's overload capacity. Tawarawala

et al. [80] quantify the effect of considering transient operations, or variable displacement, in comparison to sizing the machine based on corner power using the example of a 5-ton mini excavator's arm actuator application. They consider leveraging the overload capacity and variable displacement individually, but do not state how overheating is avoided when operation is outside the considered drive cycle, e.g., low-speed holding of a high load. That said, variable displacement could be used as a mechanism to protect the machine from overheating, by reducing displacement and consequently the torque load and stator currents when the thermal limit is approached.

After dimensioning the machine, volumes, masses, and inertia can be estimated.

4.2. Sizing of gearbox-coupled electric machines

In comparison to the authors' previous work [23], this paper also considers the option to use high-speed electric machines in combination with a gearbox, thereby reducing the torque demand on the electric machine. The speed of the PMSM differs depending on the use of a gearbox. Therefore, the optimal PMSM design varies across the concepts. A major design change between the different machines is the pole pair count p. As iron losses are modelled as the sum of power-law terms with respect to the electrical frequency, high-speed operation requires reducing the pole pair count. When reducing the pole pair count proportionally to the gear ratio, the electrical frequency remains constant. In addition to keeping the iron loss density constant, a constant electrical frequency also keeps the inverter's switching frequency constant, and therefore the inverter can be excluded from this comparison. However, at speeds above approximately 15 000 rpm, challenges with bearings, carbon-fibre banding and noise increase significantly. Accordingly, this study sets the maximum electric machine speed to 15 000 rpm.

The base machine has 5 pole pairs and a mechanical speed up to 6000 rpm. When limiting the mechanical speed to up to 15 000 rpm, machines with 4, 3, or 2 pole pairs are considered.

When modifying the pole pair count, the stator slot count also must be adjusted. The slot count per pole per phase q (see Eq. (8)) is useful to distinguish between different machine types that possess different characteristics:

- Machines with q being an integer ($q \in \mathbb{Z}$) are integer wound machines. They typically possess high winding factors, longer end windings, and lower fill factors than the following two machine types.
- Machines with q being the reciprocal of an integer ($q = \frac{1}{n}$, where $n \in \mathbb{Z}$ and $n > 1$) are brushless DC machines. They typically have a simple control, short end windings, but low winding factors. To achieve an adequate winding factor in 3-phase machines, n needs to be 2 or 4.
- For fractional slot concentrated winding (FSCW) machines, neither of the two previous criteria is met. One example for a FSCW machine is the machine dimensioned in [23]. A combination of 5 pole pairs and 12 slots achieves a winding factor 11% higher than that of BLDC machines while having a good fill factor as well as short end windings.

$$q = \frac{N_s}{2 n_{pp} n_p} \tag{8}$$

Wang and Howe [81] summarised the feasible combinations of pole pair and slot counts. This study excludes stator slot counts N_s for which $(\frac{N_s}{n_p} \mod 2) = 1$ (e.g., for $n_p = 3$, $N_s = 9$), as these would cause imbalanced radial forces on the rotor. The relevant stator slot counts for this work are as shown in Table 2.

There are some differences in the sizing of the different machines:

Table 2
Relevant combinations of pole pair and slot counts.

n_{pp}	N_s	q	Machine type	Fund. k_w [82]
2	6	0.5	BLDC	0.866
2	12	1	Integer wound	1
3	18	1	Integer wound	1
4	6	0.25	BLDC	0.866
4	12	0.5	BLDC	0.866
4	24	1	Integer wound	1
5	12	0.4	FSCW	0.933

- The calculation of the width of the stator teeth varies across the different machines. It is considered that one magnet pole spans an arc of 145°_{el}. For FSCW and BLDC machines, each tooth is dimensioned to be able to guide the maximum magnet flux under one slot pitch. For integer wound machines, the flux under load is unevenly distributed among the teeth, and wider teeth are required to avoid saturation. Therefore, the tooth width for integer wound machines is increased approximately 20% compared to the approach used for FSCW and BLDC machines.
- For integer wound machines, the FSCW machine, and BLDC machines with q=0.5, each pole's flux through the rotor is shared equally with the neighbouring poles. However, for BLDC with q=0.25, the flux distribution in the rotor yoke between neighbouring poles changes over time and is asymmetric, thus the rotor yoke is sized 50% larger. The increased rotor iron losses for this machine type have been neglected in this study.
- The end winding for FSCW or BLDC machines only spans one slot, and thus does not need to 'avoid' other end windings. For integer wound machines, the end windings cover a span of multiple slots, and thus an additional axial length is considered. Furthermore, for FSCW and BLDC machines, semi-circular end windings are assumed, whereas for integer wound machines, an empirical equation assumes a flatter shape.
- Assuming random wound machines for the FSCW or BLDC machines, and insertion winding for the integer wound machine, the fill factor for FSCW or BLDC machines is higher than for integer wound machines, as each coil can be wound individually when using segmented teeth.
- The winding factors differ for the different machines as shown in Table 2. The winding factor for BLDC is lower than for integer wound machines, reducing the effective magnetic loading of the airgap, and thus requiring a larger rotor for the same torque. For FSCW machines, the winding factor depends on the slot/pole combination [82].

For each of the configurations in Table 2, Ansys Motor-CAD [83] simulations have been carried out to validate the analytical electromagnetic calculations, and exemplary validation results are shown in Table 3. Copper loss deviations arise due to differences in the end winding computation, as the analytical method neglects the effect of the tooth tips. Further, Motor-CAD by default assumes semi-circular end windings for all machines, whereas this paper only assumes that for BLDC and FSCW machines (see the list above). Iron losses are generally difficult to estimate, and the flux density is not uniformly distributed over space and time. Additionally, the tooth tips are not considered in the analytical procedure. The deviations for losses and torque between the FEM and analytical calculations are in an acceptable range.

4.3. Sizing results

4.3.1. Machine for direct drive

Fig. 7 shows the results for the machine's main dimensions for a fixed cooling condition as a function of the airgap diameter. The figure also visualises constraints for diameters that are too small, where the hydraulic machine cannot be radially integrated within the electric

Table 3
Exemplary comparison between Finite Element Method (FEM) results and analytical calculation results. The column "diff." shows the difference between the two results in percent, with the FEM results being the baseline. The motor type shows: gear ratio/pole pair count/slot count.

	Airgap dia.	Copper loss in W			Iron loss in W			Torque in Nm		
Motor type	in mm	FEM	analytical	diff.	FEM	analytical	diff.	FEM	analytical	diff.
1.00/5/12	50	3605	3732	4%	677	912	35%	140	145	4%
1.00/5/12	80	1996	1947	−2%	718	844	17%	147	145	−2%
1.00/5/12	135	771	765	−1%	916	990	8%	145	145	0%
1.25/4/24	80	1385	1558	12%	878	777	−12%	119	116	−2%
1.25/4/12	80	1747	1700	−3%	733	730	0%	120	116	−3%
1.25/4/6	80	1604	1569	−2%	949	948	0%	115	116	1%
1.67/3/18	80	1068	1161	9%	816	717	−12%	89	87	−2%
2.50/2/12	80	728	752	3%	820	702	−14%	56	58	3%
2.50/2/6	50	1613	1632	1%	656	602	−8%	59	58	−1%
2.50/2/6	80	834	801	−4%	744	654	−12%	58	58	1%

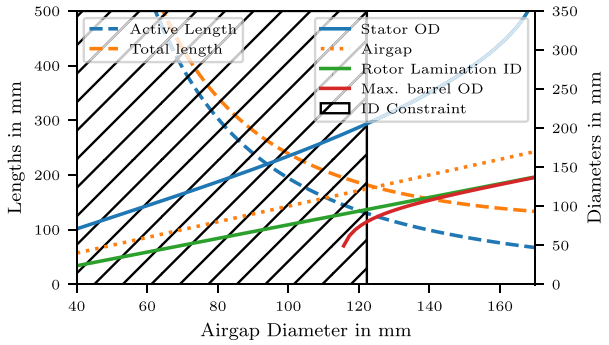

Fig. 7. PMSM machine dimensions for a 12-slot/10-pole machine as function of the airgap diameter for a fixed thermal loading.

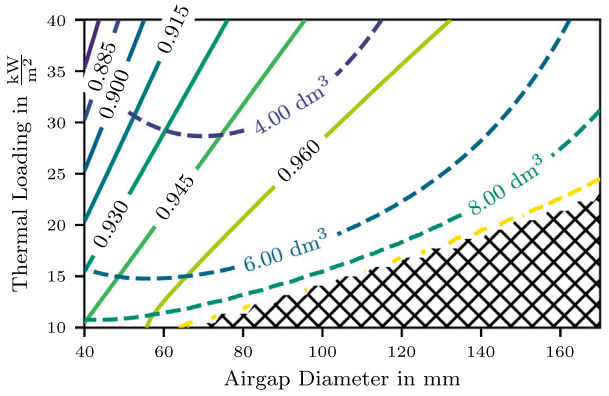

Fig. 8. 12-slot/10-pole PMSM volume and efficiency as function of airgap diameter and thermal loading. The hatched area marks infeasible combinations.

machine. Thus, the range of useful airgap diameters is limited when radially integrating a hydraulic machine within the PMSM's core.

Fig. 8 shows the volume as well as the efficiency of the 12-slot/10-pole PMSM as a function of the airgap diameter and the thermal loading (in equilibrium identical with the cooling capacity) of the machine. A higher thermal loading can allow more compact designs at the expense of decreased efficiency. Note that machines with a large airgap diameter and a low thermal loading are not feasible, as the lateral surface of the active length is not sufficient to dissipate the losses.

The water-cooled reference machine assumes a thermal loading of around 22 kW/m^2, and the same thermal loading is assumed for all other machines throughout this paper.

4.3.2. High-speed machine for drive via gearbox

Using a gear ratio leads to lower torques and higher speeds, making lower pole pair counts preferable. Fig. 9 shows the total volume and

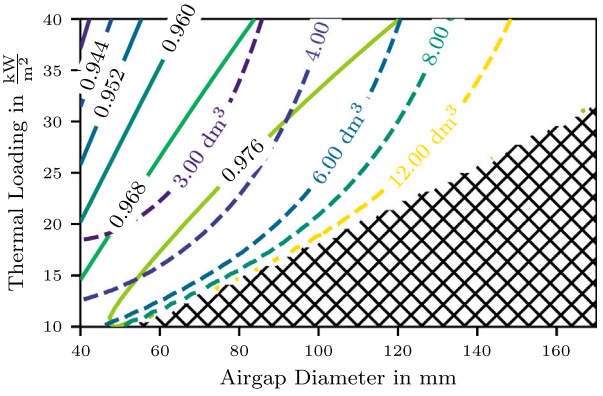

Fig. 9. 6-slot/4-pole PMSM volume and efficiency as function of airgap diameter and thermal loading. The hatched area marks infeasible combinations.

efficiency for a 6-slot/4-pole PMSM as a function of airgap diameter and the thermal loading/cooling capacity of the machine. Due to the reduced active length, cooling becomes increasingly difficult for large airgap diameters. Note also that the end windings contribute more significantly to losses for large airgap diameters, and since they are typically embedded in materials with low thermal conductivity, their contribution to cooling is neglected.

The following figures compare the different machine setups for the same heat transfer coefficient and their individual, gear-ratio-dependent torque requirements.

Fig. 10 shows the volume of the different machine setups. The volume is calculated based on the stator outer diameter, and the total axial length including end windings. The torque requirement for the gearbox-coupled machines is reduced, but the machines' volume is not reduced in proportion to the torque reduction due to the end windings' lengths. Further, the figure shows the electromagnetic efficiency at the design point for the different machine setups. The stator iron losses and the copper losses in the windings were considered for the efficiency calculation.

Fig. 11 shows the aspect ratio and total mass of the active parts of the machines. Note that there are different definitions for the aspect ratio, e.g., Lipo defined it as the active length divided by the pole pitch [75], whereas Sarode et al. [31] defined it as the ratio between the stator outer diameter and the total length of the machine. This work will follow Sarode et al.'s definition (see Eq. (9)). In the work of Sarode et al. [31], the aspect ratio was fixed as 1. The desired aspect ratios strongly depend on the mounting situation, and may vary based on whether the PMSM is placed in a central compartment, or for example on an excavator's arm in a decentralised system. The total mass is important when considering the use of the machine in decentralised systems. The total mass is computed by summing the masses of the rotor

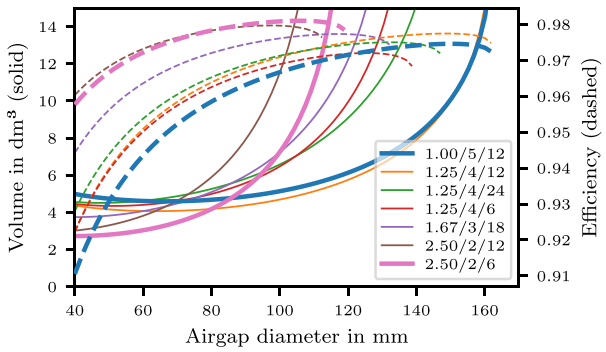

Fig. 10. PMSM volume and efficiency for different machine setups. The legend shows: gear ratio/pole pair count/slot count. The most relevant machine types used for the direct-driven and the gearbox-coupled concepts are drawn with thicker lines.

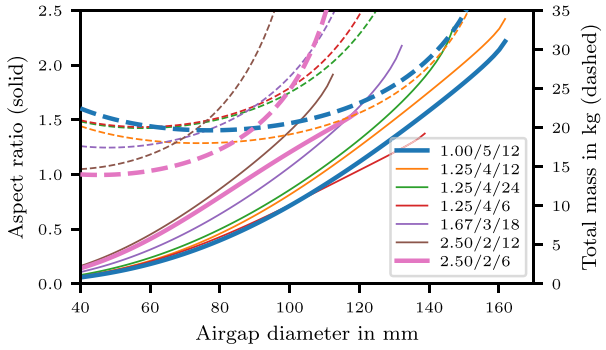

Fig. 11. PMSM aspect ratio and total mass of active parts for different machine setups. The mass computation assumes a hollow rotor and no shaft. The legend shows: gear ratio/pole pair count/slot count.

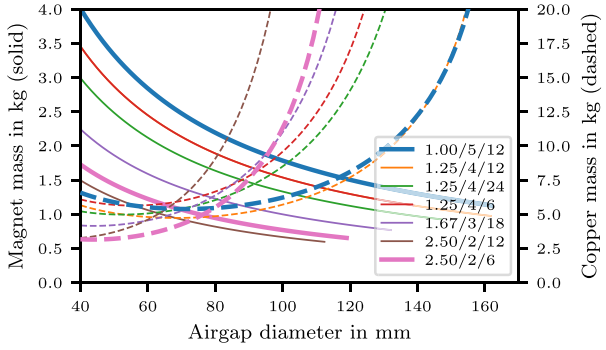

Fig. 12. PMSM magnet and copper mass for different machine setups. The legend shows: gear ratio/pole pair count/slot count.

and stator iron, the copper windings, and the magnets. Bearings, shaft, and housing are neglected.

$$\text{AspectRatio} = \frac{D_{\text{machine}}}{l_{\text{machine}}} \tag{9}$$

Fig. 12 shows the magnet and the copper mass for the different machine setups. Both rare earth magnetic materials and copper are of limited availability, and their cost relative to other materials can increase significantly. In addition, there is both social and environmental concern about the sourcing of rare earth materials. Therefore, designs using less of these materials are advantageous.

Fig. 13 shows the rotor inertia for the different machine setups, as well as the equivalent inertia at the hydraulic machine shaft when

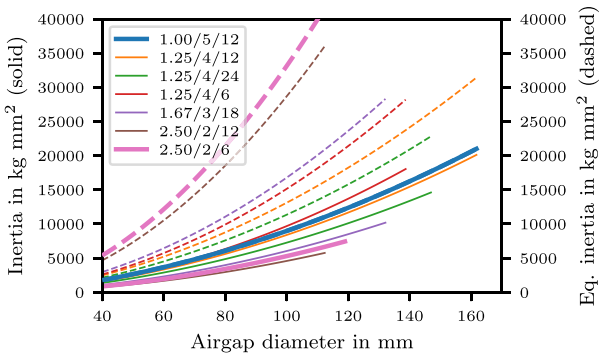

Fig. 13. PMSM rotor inertia as well as reduced rotor inertia to the hydraulic machine reference, both assuming a hollow rotor. The legend shows: gear ratio / pole pair count / slot count.

considering the gear ratios. Lower inertia is desirable for improved motor dynamic response. When using a gearbox, the equivalent inertia J_{eq} of the electric machine referred to the hydraulic machine's shaft follows Eq. (10). For the same airgap diameter, the equivalent inertia of the machines using a gearbox is consequently higher.

$$J_{\text{eq}} = J \cdot u^2 \tag{10}$$

4.4. Discussion

As expected, the results show that the lowest PMSM volumes can be achieved for the highest gear ratios (due to the reduced torque requirement). The 6-slot/4-pole machine shows a higher compactness and efficiency than the 12-slot/4-pole machine, making the 6-slot/4-pole machine the most promising candidate for an integration with a gearbox. Although the volume of the gearbox-coupled PMSM is reduced due to the lower torque requirement, the reduction is not proportional because of the end windings. The most compact designs possess very low aspect ratios, resulting in very long and thin machines. Such low aspect ratios are very unusual, and come with additional challenges for manufacturing and rotor stability. The compactness is reduced for larger aspect ratios. 6-slot/4-pole machines with large airgap diameters require an increased cooling effort due to their low active length. Note that the heat conductivity at the active length is highest, and very low for the end windings. Therefore, only the heat transfer over the active length is considered in this work.

The copper and magnet mass can be significantly reduced through the use of a gearbox, whereas the equivalent inertia and total mass are not significantly reduced in comparison to the direct-driven concepts.

For the concept comparison, the 12-slot/10-pole machine is considered for the direct-driven concepts, and the 6-slot/4-pole machine is considered for the gearbox-coupled concepts.

5. Gearbox design

As mentioned in Section 2, planetary gearboxes are highly compact and efficient, with coaxial input and output shafts [16]. Therefore, they are chosen in this study.

5.1. Gearbox concept

Previous work by the authors [23] considered electro-hydraulic energy converters with a displacement of 35 cc/rev spinning at 6000 rpm. Note the scaling law in Eq. (3) stating that larger displacements reduce the maximum speed capability, and therefore do not yield a linearly increasing flow capacity. To provide a comparison to those results, the maximum speed of the hydraulic machine is kept constant. With a

Table 4
Planetary gearbox ratios and planet diameter.

	Fixed sun	Fixed carrier	Fixed ring gear
Gear ratio i	1-1/($i_{operatorname02}$)	i_{02}	1-i_{02}
d_1	$\frac{-d_0}{2}\left(1+\frac{1}{1-i}\right)$	$-d_0\frac{1+i}{2}$	$-d_0\left(1-\frac{i}{2}\right)$
d_1 for $\lvert i\rvert = 2.5$	$\frac{9}{14}d_0$	$\frac{3}{4}d_0$	$\frac{1}{4}d_0$

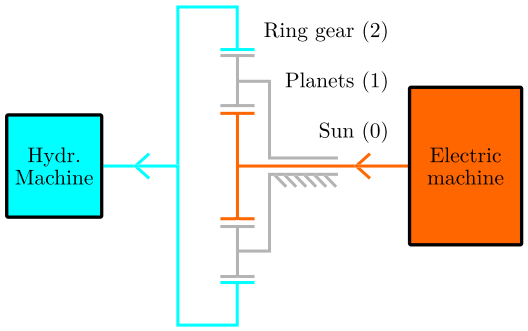

Fig. 14. Sketch of planetary gearbox concept with fixed planetary carrier.

maximum e-machine speed of 15 000 rpm (see Section 4.2), this implies a gear ratio of 2.5 for the planetary gearbox, which is similar to those used by Pietrzyk et al. [16] and Lindh et al. [65], who used gear ratios of 3.

Planetary gearboxes have different ratios depending on which gear, if any, is held stationary. The general relationship for speeds of planetary gear carriers is given in Eq. (11) [4], with the rotational speed of the sun n_0, the rotational speed of the carrier shaft n_1, the rotational speed of the ring gear n_2 and the tooth count ratio of the sun and the ring gear i_{02}. Eq. (12) gives the tooth count ratio of the sun and the ring gear i_{02} as the ring gear's tooth count z_2 divided by the sun's tooth count z_0. This work only considers planetary gearboxes with a fixed gear, simplifying Eq. (11) to the cases given in Table 4.

$$n_0 - n_2 i_{02} - n_1(1 - i_{02}) = 0 \tag{11}$$

$$i_{02} = \frac{z_2}{z_0} \tag{12}$$

Eq. (13) gives the relationship between the diameters of the sun, the planets, and the ring gear. Note that the diameters of internal gears are defined as negative.

$$d_0 + 2d_1 = -d_2 \tag{13}$$

Combining Eqs. (12) and (13) with the first line of Table 4 yields the expressions in the second and third line of Table 4. Using the sun as input and the planet carrier shaft as output (i.e., using a fixed ring gear) would lead to very small planets at a gear ratio of ±2.5 (note that fixing the sun or carrier yields a negative gear ratio, while fixing the ring gear results in a positive one). Therefore, it is more advantageous to connect the sun gear to the electric machine, and the ring gear to the hydraulic machine as sketched in Fig. 14. Further, this setup avoids challenges due to a rotating carrier shaft such as centrifugal forces, splashing losses, and lubrication problems [16].

5.2. Gear sizing

Typical failure causes for gears are tooth bending, Hertzian stress, and scuffing. Gears have been extensively researched, and national as well as international standards use physical and empirical factors in their sizing. One of the most relevant standards is ISO 6336 [84]. The standard applies engineering equations such as contact stress or bending stress in combination with influence factors. These influence factors can among others depend on the gear geometry, the manufacturing processes, and the intended application. Some of the influence factors affect other influence factors. There are different methods for calculating the influence factors, depending on the available data and desired level of accuracy. Furthermore, safety factors are applied.

5.2.1. Hertzian stress

ISO 6336-2 [85] provides the calculation of the surface durability of the gear flank. The calculation is based on the contact stress at the pitch point. The standard is based on Hertzian theory and applies influence factors accounting for the geometry and application.

The safety factors S_{Ha} and S_{Hb} compare the pinion's contact stress σ_{Ha} and the wheel's contact stress σ_{Hb} with the corresponding material properties σ_{HGa} and σ_{HGb}, see Eq. (14).

$$S_{\mathrm{Ha}} = \frac{\sigma_{\mathrm{HGa}}}{\sigma_{\mathrm{Ha}}} > S_{\mathrm{Hmin}} \tag{14a}$$

$$S_{\mathrm{Hb}} = \frac{\sigma_{\mathrm{HGb}}}{\sigma_{\mathrm{Hb}}} > S_{\mathrm{Hmin}} \tag{14b}$$

The nominal contact stress σ_{H0} in the pitch point assumes flawless gearing and static torque and is computed according to Eq. (15), with the tangential force F_{t}, the pinion reference diameter d_{a}, the face width b, the gear ratio u, and the influence factors Z which account for geometry and material properties.

$$\sigma_{\mathrm{H0}} = Z_{\mathrm{H}} \cdot Z_{\mathrm{E}} \cdot Z_{\varepsilon} \cdot Z_{\beta} \cdot \sqrt{\frac{F_{\mathrm{t}}\left(\frac{u+1}{u}\right)}{d_{\mathrm{a}} b}} \tag{15}$$

Eq. (16) applies further influence factors Z and K to the nominal pitch point contact stress σ_{H0}. $Z_{\mathrm{B,D}}$ convert the contact stress at the pitch point to the determinant contact stress σ_{H}. The influence factors K account for application conditions, internal dynamics, and uneven load distribution (e.g., due to manufacturing inaccuracies or elastic deformation) to calculate the contact stresses σ_{H}.

$$\sigma_{\mathrm{Ha}} = Z_{\mathrm{B}} \cdot \sigma_{\mathrm{H0}} \cdot \sqrt{K_{\mathrm{A}} \cdot K_{\gamma} \cdot K_{\mathrm{v}} \cdot K_{\mathrm{H}\beta} \cdot K_{\mathrm{H}\alpha}} \tag{16a}$$

$$\sigma_{\mathrm{Hb}} = Z_{\mathrm{D}} \cdot \sigma_{\mathrm{H0}} \cdot \sqrt{K_{\mathrm{A}} \cdot K_{\gamma} \cdot K_{\mathrm{v}} \cdot K_{\mathrm{H}\beta} \cdot K_{\mathrm{H}\alpha}} \tag{16b}$$

The determinant contact stress σ_{H} is compared to a permissible contact stress σ_{HP} (see Eq. (17)) to evaluate the surface durability of the gear flanks.

$$\sigma_{\mathrm{HP}} = \frac{\sigma_{\mathrm{Hlim}} \cdot Z_{\mathrm{NT}}}{S_{\mathrm{Hmin}}} \cdot Z_{\mathrm{L}} \cdot Z_{\mathrm{V}} \cdot Z_{\mathrm{R}} \cdot Z_{\mathrm{W}} \cdot Z_{\mathrm{X}} = \frac{\sigma_{\mathrm{HG}}}{S_{\mathrm{Hmin}}} \tag{17}$$

If the surface durability of the gear is insufficient, small particles break loose, also known as *pitting*. This process can cause increased noise and can progress until gear failure.

5.2.2. Tooth bending

ISO 6336-3 [86] provides the calculation method for the tooth bending strength of gears.

Safety factors $S_{\mathrm{Fa,b}}$ compare the tooth root stress of the pinion and the wheel $\sigma_{\mathrm{Fa,b}}$ against the corresponding material properties σ_{FGa} and σ_{FGb}, see Eq. (18).

$$S_{\mathrm{Fa}} = \frac{\sigma_{\mathrm{FGa}}}{\sigma_{\mathrm{Fa}}} \geq S_{\mathrm{Fmin}} \tag{18a}$$

$$S_{\mathrm{Fb}} = \frac{\sigma_{\mathrm{FGb}}}{\sigma_{\mathrm{Fb}}} \geq S_{\mathrm{Fmin}} \tag{18b}$$

The widely applied calculation method B in ISO 6336 determines the nominal tooth root stress σ_{F0} based on the tangential force F_t distributed on the area of the tooth width b and the modulus m, and various influence factors Y based on geometry and application as shown in Eq. (19). σ_{F0} assumes flawless gearing and static torque.

$$\sigma_{F0} = \frac{F_t}{b \cdot m_n} \cdot Y_F \cdot Y_S \cdot Y_\beta \cdot Y_B \cdot Y_{DT} \tag{19}$$

Eq. (20) calculates the tooth root stress σ_F as the product of the nominal tooth root stress σ_{F0} and the influence factors K.

$$\sigma_F = \sigma_{F0} \cdot K_A \cdot K_\gamma \cdot K_v \cdot K_{F\beta} \cdot K_{F\alpha} \tag{20}$$

Eq. (21) calculates the permissible bending stress.

$$\sigma_{FP} = \frac{\sigma_{Flim} \cdot Y_{ST} \cdot Y_{NT}}{S_{Fmin}} \cdot Y_{\delta relT} \cdot Y_{RrelT} \cdot Y_X \tag{21}$$

If the tooth bending strength is exceeded, tooth breakage occurs which usually results in sudden gearbox failure. Consequently, ISO 6336-3 recommends selecting a higher safety factor for tooth bending than for pitting.

5.2.3. Scuffing

For thin lubrication films, asperity contact occurs, and thus adhesive wear becomes possible. Adhesive wear occurs via localised welding, leading to particle detachment and transfer from the gear teeth. Scuffing refers to severe adhesive wear in gear contacts [87].

Scuffing is caused by high contact temperatures of the fluid or the flanks, which cause a breakdown of the lubrication film. The contact temperature is the sum of the bulk temperature and the flash temperature of the moving faces in contact. The flash temperature fluctuates rapidly and depends on geometry, load, friction, velocity, and material properties [87].

ISO 6336-20 [87] and 6336-21 [88] calculate the scuffing load capacity with the flash temperature method and the integral temperature method, respectively. The difference between the two methods is that the flash temperature method considers a varying temperature along the contact paths, whereas the integral temperature method considers a weighted sum of the temperatures along the contact paths [88]. Both methods calculate the safety factor as the ratio of the limiting temperature to the calculated temperature.

Scuffing risk is increased by aeration or contamination of the lubricant. Even brief transient overloading can result in scuffing failure [87].

5.2.4. Commercial software

Commercial software performs gear calculations in accordance with the standards. In this work, the planetary gear train module in the eAssistant by GWJ Technology GmbH was used [89]. The planetary gear train was calculated in accordance with ISO 6336:2019 Method B for pitting and tooth bending, and in accordance with ISO TR 13989 [90,91] for the scuffing safety.

5.2.5. Assumptions/simplifications

This work simplifies the planetary gear train by using spur gears, i.e., the helix angle β is 0°. This provides the following advantages: simplified calculation, low axial bearing loads, and easier assembly. Helical gears could offer increased compactness and reduced noise in comparison to spur gears due to the extended contact line allowing multiple teeth to engage simultaneously. However, the increased compactness for helical gears only applies if the extended contact lines are fully used, which can be hindered by manufacturing tolerances and elastic deformation of the teeth and the shaft/bearing systems [92]. Further, helical gears introduce axial loads to the bearings.

A parameter sweep is performed in Section 5.2.6 to justify further simplifications, and parameters for a detailed gear design are shown in Section 5.2.7. The parameters defined in the detailed design are used for the simplified calculations. Both the parameter sweep and the detailed design were carried out using the GWJ eAssistant as described in Section 5.2.4.

Table 5
Some assumptions/inputs for parameter sweep gear calculation.

Symbol	Meaning	Value
i	Gearbox ratio	−2.5
n	Output speed	6000 rev/min
K_A	Application factor	1.35
K_γ	Mesh load factor	1.0
N_p	Number of planets	3
P	Output power	122.5 kW
T	Output torque	195 Nm
Y_B	Rim thickness factor	1.0
Y_{DT}	Deep tooth factor	1.0
Y_{NT}	Life factor	0.85
Y_{RrelT}	Relative surface factor	0.97
Y_{ST}	Stress correction factor	2.0
Y_X	Size factor	1.0
Y_β	Helix angle factor	1.0
Z_B, Z_D	Tooth contact factor	1.0
Z_E	Elasticity coefficient	193.9 $(N/mm^2)^{0.5}$
Z_L	Lubricant factor	0.97
Z_{NT}	Life factor	0.85
Z_W	Work hardening factor	1.0
Z_X	Size factor	1.0
Z_β	Helix angle factor	1.0
β	Helix angle	0 rad

Table 5 summarises some assumptions and inputs related to the gear calculation, as well as factors that remain constant for the parameter sweep.

5.2.6. Parameter sweep

One set of calculations was carried out sweeping through different moduli, sun gear tooth counts, and gear widths as independent variables. The parameter sweep included the moduli 1, 1.5, and 2 mm, sun gear tooth counts from 16 to 80, and gear widths from 16 to 50 mm. For each of the gears, case hardened steel (16MnCr5) was assumed to be the material. The gear ratio was fixed to −2.5, and the number of planets was 3. The other diameters and gear tooth counts were calculated from those parameters. Profile shifts of 0 were entered into the software. Using no profile shift does not use the full potential of the gearbox, but gives insight into general trends and approximate sizes.

As a simplification, this paper combines all the influence parameters into a single global parameter for each contact. For example, Eq. (22) introduces $K_{F,ij}$ for tooth bending for the gears i and j (e.g., between sun (index 0) and planet (index 1)) and Eq. (23) defines $K_{H,ij}$ for pitting in the contact between sun (index 0) and planet (index 1). Similarly, the corresponding equations for the other contacts are defined. However, for some designs, the software introduced non-zero profile shifts, leading to less smooth results in Fig. 15.

$$K_{F,01} = \frac{N_p b m^2 \sigma_{Flim0} z_0}{2 S_{F01} \cdot T_0} \tag{22}$$

$$K_{H,01} = \frac{\sigma_{Hlim0}\sqrt{b d_1}}{S_{H01}\sqrt{\frac{F_{t01}(u_{01}+1)}{u_{01}}}} = \frac{\sqrt{2}\sigma_{Hlim0}\sqrt{bm\left(\frac{-iz_0}{2} - \frac{z_0}{2}\right)}}{S_{H01} \cdot 2\sqrt{\frac{T_0\left(\frac{-iz_0}{2} - \frac{z_0}{2}\right)\left(\frac{z_0}{\frac{-iz_0}{2} - \frac{z_0}{2}} + 1\right)}{N_p m z_0^2}}} \tag{23}$$

Fig. 15 visualises the results of the parameter sweep for the summarised influence factors expressed as a percentage of the fixed values from the full design. The figure shows that despite very large variation in gearbox volume (with the smallest and the largest volume differing

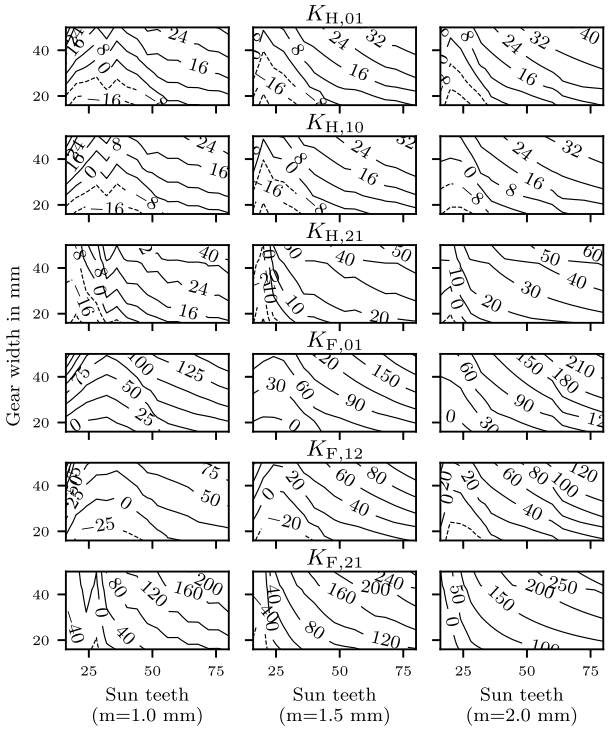

Fig. 15. Deviation in percent of summarised influence factors resulting from parameter sweep to the fixed values in Table 6.

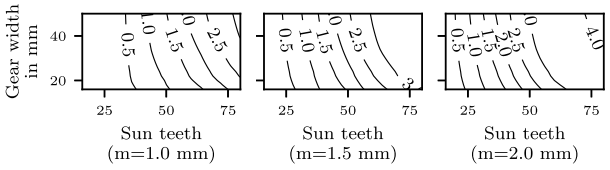

Fig. 16. Minimum scuffing safety results according to the integral temperature method for parameter sweep.

by a factor greater than 50), the summarised K factors vary significantly less. Furthermore, the factor with the largest deviation ($K_{F,21}$) has the largest safety factors as shown in Fig. 18. This justifies treating the summarised K factors as constant in the proximity of a feasible solution.

Furthermore, Fig. 16 shows the scuffing safety results according to the integral temperature method for the parameter sweep. The results indicate that higher gear tooth counts and larger moduli improve scuffing safety. The results for the flash temperature method are not shown here, since the safety factors were significantly higher than those from the integral temperature method and therefore not critical for sizing considerations.

Fig. 17 shows efficiency results for the parameter sweep. The total gearbox efficiency η_{gearbox} is calculated as the product of the efficiencies of the sun-planet contact η_{01}, and of the planet-ring gear contact η_{12}.

$$\eta_{\text{gearbox}} = \eta_{01} \cdot \eta_{12} \tag{24}$$

Literature gives some rules of thumb for gearbox efficiency, e.g., 0.5% to 1% loss per gearing stage. Typically, outer gear contacts have efficiencies of around 0.99, and contacts between internal and external gears around 0.995. This results in an overall gear efficiency of approximately 0.985 [4] when the carriers are fixed. The figure shows slightly higher efficiencies than expected according to the Refs. [4,92], and one can see a trend of higher efficiencies with greater gear tooth counts. However, this only considers the losses due to the gear contact, and neglects other losses such as bearing friction and churning losses.

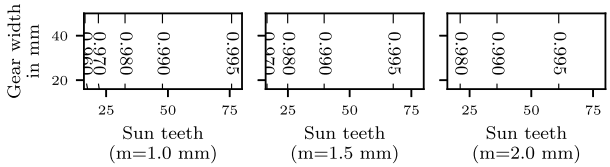

Fig. 17. Efficiency results for parameter sweep.

Table 6
Summarised influence factors for gear sizing.

Symbol	Meaning	Value
$K_{H,01}$	Pitting of sun in contact with planet	965 $\sqrt{\text{N}}$/mm
$K_{H,10}$	Pitting of planet in contact with sun	1003 $\sqrt{\text{N}}$/mm
$K_{H,21}$	Pitting ring gear in contact with planet	971 $\sqrt{\text{N}}$/mm
$K_{F,01}$	Tooth bending sun in contact w. planet	5.86
$K_{F,12}$	Tooth bend. planet in cont. w. ring gear	8.85
$K_{F,21}$	Tooth bend. ring gear in cont. w. planet	8.10

5.2.7. Summarised influence factors

Assuming constant summarised influence factors near the design point, alternative designs can be explored. Fig. 15 shows the summary of the influence factors for the parameter sweep carried out in Section 5.2.6. The minimum and maximum values for K_{H} differ by a factor of less than 2, and the minimum value and the maximum value for K_{F} differ by a factor of less than 3 when neglecting some values at the very low end. This variation is small considering that the gearbox volume for the considered parameters varies by a factor of more than 50, and supports treating the summarised K factors as constant for designs in the proximity of the detailed design.

A detailed design including profile shift and micro-geometry modifications has created to extract reasonable values for the summarised K factors. The materials used were case-hardened 16MnCr5 steel for sun and planets, and 31CrMoV9 nitrided steel for the ring gear, since nitriding is a commonly applied surface treatment for ring gears. The summarised influence factors given in Table 6 were extracted from the detailed design and applied in this work. For the given summarised influence factors, Eqs. (22) and (23) can compute the safety factors.

For the detailed design, scuffing safety was also considered. However, no simple scaling parameter for scuffing was implemented, but Fig. 16 can be used to derive trends for scuffing safety depending on modulus, sun tooth counts, and gear width.

5.3. Planet carrier sizing

Besides the gears, the planet carrier is considered as an active part. Planet carriers transfer the forces of each planet as torque. Most commonly, planet carriers consist of two discs, positioned on either side of the planet gears and aligned parallel to each other [93,94]. This is advantageous for heavy load transmissions due to increased stiffness and loading capacity compared to single-sided support of the planet gears [94]. The discs are connected to one another by arms using the space between the planets. In the case of a stationary carrier, one of the discs is connected to the housing [93].

Jacobs et al. [22,95] present sections of their axially stacked machine including a gearbox. From the sections, the carrier width can be approximated as 80% of the gear width, and therefore the width of the planetary carrier is computed using Eq. (25). Eq. (26) is then used to calculate the axial length of the gearbox. Furthermore, linear scaling is used to estimate the carrier's inner and outer diameter to subsequently compute its mass.

$$b_{\text{carrier}} = 0.8 \cdot b \tag{25}$$

$$l_{\text{gearbox}} = b + b_{\text{carrier}} \tag{26}$$

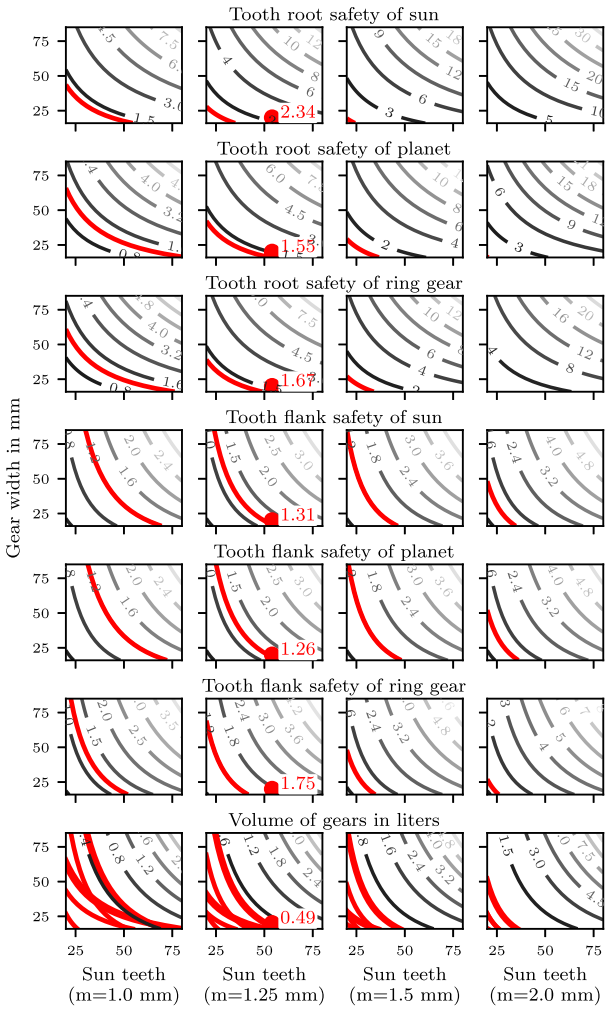

Fig. 18. Safeties for each contact assuming fixed summarised influence factors (see Table 6). The point of the detailed design which is the base for the influence factors is marked with a red dot, and the safety factor constraints are marked in red.

5.4. Sizing results

Fig. 18 shows the safety factors as a function of modulus, sun gear tooth counts, and gear width. For each contact, the required safety for pitting and tooth bending are indicated by red lines. The final row of plots combines the constraints across all gear contacts.

Fig. 19 shows the corresponding outer dimensions for the gearbox, including the carrier. The volume and mass of feasible gearboxes remain relatively constant.

5.5. Noise

Variation in the number of contacting gear teeth leads to fluctuating contact stiffness and is a major source of noise in gearboxes. Thus, gearbox design aims to maintain a constant whole number of teeth in contact. The number of contacting gear teeth ε_γ can be divided into the teeth in contact for a spur gear ε_α, and additionally the gears in contact due to a helix angle ε_β, see Eq. (27).

$$\varepsilon_\gamma = \varepsilon_\alpha + \varepsilon_\beta \tag{27}$$

Since spur gears were assumed, the helix contribution ε_β equals zero. For the detailed design (see Section 5.2.7), the objective of achieving an integer value for ε_γ was not met, with the contact number

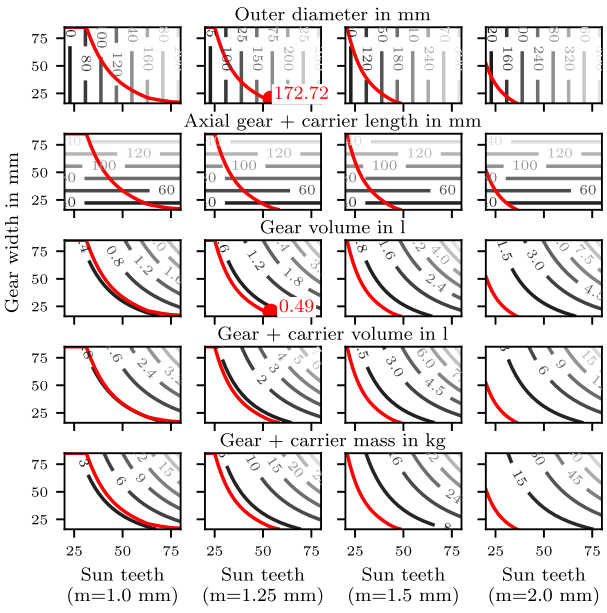

Fig. 19. Visualisation of feasible gear widths, outer diameters, additional axial lengths for the carrier, gear volume, active volume including the carriers, and mass of active parts. The point of the detailed design which is the base for the influence factors is marked with a red dot, and the safety factor constraints are marked in red.

of the contact between sun and planet $\varepsilon_{\gamma,01}$ being 1.66 and the contact number between planet and ring gear $\varepsilon_{\gamma,12}$ being 1.82.

6. Integrated machines

Five integration concepts as shown in Fig. 1 are considered. For the hydraulic machine topology, based on findings reported in previous work [23], a floating piston machine has been selected. The floating piston machine's compactness increases with its swash angle, however its swash angle is limited to approximately 8°. Thus, a swash angle of 8° is chosen, and the piston count serves as the free variable determining the machine's length and outer diameter (see Fig. 5). Both conventional single pumps and double pumps with mirrored rotating groups are considered.

For the direct-driven machines, 12-slot/10-pole PMSMs (see Fig. 7) were chosen. For the machines using a gearbox, a gear ratio of −2.5 (see Section 5.1) and 6-slot/4-pole PMSMs have been selected (see Section 4.4). For both PMSMs, the same fixed heat transfer coefficient is assumed.

For all machines, the volume is calculated according to Eq. (28). The following section explains how the relevant lengths and diameters are determined for each machine type. Only the diameter and length of the active parts are quantified, whereas housings and similar parts are not considered.

$$V = \frac{\pi\, l_{\text{machine}}\, D^2_{\text{machine}}}{4} \tag{28}$$

6.1. Direct-driven, axially stacked machines

For the direct-driven, axially stacked machine, Eq. (29) is used to calculate the machine's outer diameter and total length. The total volume is defined by the sum of the lengths of the hydraulic and electric machines, and the largest outer diameter as sketched in Fig. 1(a).

$$D_{\text{machine}} = \max(OD_{\text{PMSM}}, OD_{\text{HM}}) \tag{29a}$$

$$l_{\text{machine}} = l_{\text{PMSM}} + l_{\text{HM}} \tag{29b}$$

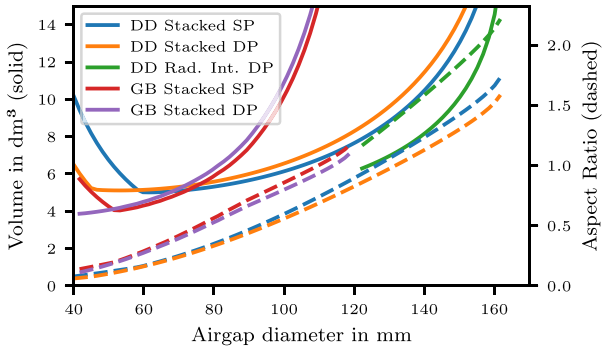

Fig. 20. Total volume and aspect ratio of the different concepts. DD — direct-driven, GB – gearbox-coupled, SP — single pump, DP — double pump.

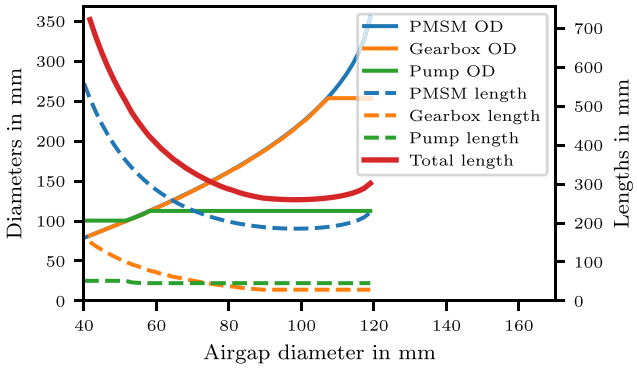

Fig. 21. Lengths and diameters of axially stacked, gearbox-coupled machine using a floating piston machine of single pump type.

Fig. 20 shows the resulting volumes and aspect ratios for the different machine concepts. For the axially stacked, direct-driven concept, the single pump type, which features a larger diameter and shorter axial length compared to the double pump type (see Fig. 5), is more compact than the double pump type when paired with medium or large airgap diameters due to a reduced diameter mismatch between the PMSM and the hydraulic machine.

6.2. Direct-driven, radially integrated machines

For the direct-driven, radially integrated machine, the volume is defined by the electric machine's stator outer diameter and the greater of the hydraulic or electric machine lengths, see Fig. 1(b) and Eq. (30). However, the radial integration is feasible only if the electric machine's rotor inner diameter is larger than the hydraulic machine's barrel diameter, and therefore only hydraulic machines of double pump type (see Fig. 3(b)) are considered. Additionally, the allowable outer diameter of the hydraulic machine is further constrained, as a tube must be placed between the hydraulic machine's barrel and electric machine's rotor to isolate the electric machine from the hydraulic machine's radial forces. Fig. 20 includes the volumes and aspect ratios of the direct-driven, radially integrated machines.

$$D_{\text{machine}} = OD_{\text{PMSM}} \tag{30a}$$

$$l_{\text{machine}} = \max(l_{\text{PMSM}}, l_{\text{HM}}) \tag{30b}$$

6.3. Axially stacked, gearbox-coupled machines

Eq. (31) defines the calculation of the diameter and length for an axially stacked, gearbox-coupled machine as sketched in Fig. 1(c). A practical design heuristic for compact axially-stacked machines is to match the outer diameters of the electric machine, the hydraulic machine and the gearbox. Then, for each individual machine, the machine with the shortest length that satisfies the outer diameter constraint is selected.

$$D_{\text{machine}} = \max(OD_{\text{PMSM}}, OD_{\text{HM}}, OD_{\text{gearbox}}) \tag{31a}$$

$$l_{\text{machine}} = l_{\text{PMSM}} + l_{\text{HM}} + l_{\text{gearbox}} \tag{31b}$$

To realise a gear ratio of −2.5, Fig. 19 shows different combinations of feasible gearbox lengths and outer diameters that achieve the desired ratio. From these options, the most compact feasible version is selected.

Figs. 18 and 19 show that as long as tooth flank safety is the main limitation, the resulting outer diameter and gear width combinations remain consistent across all moduli. However, when tooth root safety is the main limitation, higher moduli enable smaller gear widths for the same outer diameter. Furthermore, Fig. 16 shows that for the same outer diameter and gear width, the scuffing safety improves for smaller moduli. Thus, when the smallest considered modulus (m=1.0 mm) is mainly constrained by flank safety, the smallest modulus is selected. If the smallest modulus is mainly constrained by tooth root safety, the next larger modulus is selected.

For the considered machine sizes, the hydraulic machine's outer diameter for the double pump hydraulic machine is significantly smaller than the PMSM's outer diameter for almost all airgap diameters. Therefore, as illustrated in Fig. 20, the single pump configuration is more compact than the double pump configuration for almost all airgap diameters. Note also that Fig. 9 shows that the thermal equilibrium cannot be sustained under the given cooling conditions at large airgap diameters, and thus Fig. 20 does not contain results for those airgap diameters.

Fig. 21 shows the outer diameters and lengths of each component within the axially stacked, gearbox-coupled machine configuration, and the overall length.

6.4. Radially integrated, gearbox-coupled machines

Eq. (32) shows the computation of the diameter and length for radially integrated, gearbox-coupled machine as sketched in Fig. 1(d). However, for a radial integration, the outer diameters of both the gearbox and hydraulic machine must remain smaller than the inner diameter of the support tube. This tube isolates the electric machine's rotor from radial forces generated by the hydraulic machine. Therefore, a radial integration requires large airgap diameters, but the high-speed machine proved infeasible under the given cooling conditions, as its shortened active length limited the available cooling surface.

$$D_{\text{machine}} = OD_{\text{PMSM}} \tag{32a}$$

$$l_{\text{machine}} = \max(l_{\text{PMSM}}, l_{\text{HM}} + l_{\text{gearbox}}) \tag{32b}$$

6.5. Radial integration of the gearbox, and axial stacking of the hydraulic machine

Eq. (33) shows the computation of the diameter and length for machines that radially integrate the gearbox into the electric machine, and axially stack the hydraulic machine onto this as sketched in Fig. 1(e). The gearbox's outer diameter must be smaller than the PMSM's inner diameter to allow this integration. However, for the considered high-speed machine and cooling condition, no machine offers both an adequate inner diameter to accommodate the gearbox and an active length sufficient to maintain thermal equilibrium.

$$D_{\text{machine}} = \max(OD_{\text{PMSM}}, OD_{\text{HM}}) \tag{33a}$$

$$l_{\text{machine}} = \max(l_{\text{PMSM}}, l_{\text{gearbox}}) + l_{\text{HM}} \tag{33b}$$

Table 7
Selected results for integrated machines. The EHEC diameters and lengths are according to Eqs. (29) to (31). The power density of the active parts describes the continuous output power density of the active parts under consideration of electromagnetic and gearing efficiency, neglecting volumes of housings etcetera. Gearing efficiencies are approximated using Fig. 17.

(a) Results for minimal volume of each concept.

	Direct-Driven Stacked with Single Pump	Stacked with Double Pump	Radially Integrated	Gearbox-Coupled Stacked
EHEC volume	5.0 dm^3	5.1 dm^3	6.3 dm^3	3.9 dm^3
EHEC length	588 mm	774 mm	181 mm	736 mm
EHEC OD	104 mm	92 mm	211 mm	82 mm
Power density (active parts)	12.6 kW/l	12.2 kW/l	10.3 kW/l	16.2 kW/l
EHEC aspect ratio	0.18	0.12	1.17	0.11
PMSM aspect ratio	0.19	0.13	1.17	0.16
Airgap diameter	61.4 mm	53.2 mm	122.3 mm	41.6 mm
Efficiency	94.5%	93.5%	97.2%	94.0%
Electromagnetic efficiency	94.5%	93.5%	97.2%	96.0%
Gearing efficiency	–	–	–	97.9%

(b) Results for the same outer diameter as most compact direct-driven, radially integrated design.

	Direct-Driven Stacked with Single Pump	Stacked with Double Pump	Radially Integrated	Gearbox-Coupled Stacked
EHEC volume	7.9 dm^3	8.6 dm^3	6.3 dm^3	9.1 dm^3
EHEC length	226 mm	245 mm	181 mm	260 mm
EHEC OD	211 mm	211 mm	211 mm	211
Power density (active parts)	8.2 kW/l	7.6 kW/l	10.3 kW/l	7.2 kW/l
EHEC aspect ratio	0.93	0.86	1.17	0.81
PMSM aspect ratio	1.17	1.17	1.17	1.14
Airgap diameter	122.3 mm	122.3 mm	122.3 mm	96.8 mm
Efficiency	97.2%	97.2%	97.2%	97.5%
Electromagnetic efficiency	97.2%	97.2%	97.2%	98.1%
Gearing efficiency	–	–	–	99.4%

(c) Results for the same aspect ratio as most compact direct-driven, radially integrated design.

	Direct-Driven Stacked with Single Pump	Stacked with Double Pump	Radially Integrated	Gearbox-Coupled Stacked
EHEC volume	9.6 dm^3	11.9 dm^3	6.3 dm^3	–
EHEC length	210 mm	224 mm	181 mm	–
EHEC OD	242 mm	260 mm	211 mm	–
Power density (active parts)	6.8 kW/l	5.5 kW/l	10.3 kW/l	–
EHEC aspect ratio	1.15	1.16	1.17	–
PMSM aspect ratio	1.47	1.63	1.17	–
Airgap diameter	135.4 mm	142.0 mm	122.3 mm	–
Electromagnetic efficiency	97.4%	97.4%	97.2%	–

6.6. Selected results

Table 7 provides numerical values for selected designs. Table 7a shows the main dimensions, the continuous power density of the active parts, the aspect ratio, and the electromagnetic and gearing efficiency for the most compact configuration of each machine concept. Note that the power density only considers the active parts and neglects other parts such as housings. Also, the power density refers to the continuous power density. Peak power densities are higher but of less interest for dimensioning. The most compact configurations of each concept are illustrated in Fig. 22. Table 7b compares the same parameters for solutions at the same outer diameter as the most compact direct-driven, radially integrated machine. Finally, Table 7c compares the parameters for aspect ratios very close to that of the most compact direct-driven, radially integrated machine.

7. Discussion

This section summarises limitations of this study, analyses the results presented in the previous sections, and compares the various design concepts.

7.1. Limitations

The paper uses analytical equations to facilitate concept comparisons, aiming to give insights into which concept is most favourable to pursue for prototyping and testing. However, as this paper does not include prototype testing, some phenomena such as cavitation, bearing friction, churning losses, and vibrations of the components are not quantitatively considered.

Further, this study was conducted for a specific displacement and power level.

The comparison considers a single fixed heat transfer coefficient for the electric machines. This heat transfer coefficient is assumed to be independent of the machine's geometry, and local hotspots are omitted. In addition, the volumes of the cooling system and inverter are omitted. Note that for the inverter, different methods of integration with the electric machine can increase the system's power density [70]. Further, it was neglected that the centrifugal forces on the carbon-fibre banding increase significantly for high-speed machines with high airgap diameters, which could require increased airgap lengths to give space for thicker banding.

The sizing process considers only active components, omitting elements such as housings and bearings. Using off-the-shelf components results in reduced compactness compared to integrating purpose-built components, and this reduction in compactness is not quantified in the present analysis. Furthermore, when comparing direct-driven and gearbox-coupled concepts, the compactness of gearbox-coupled concepts is likely overestimated due to the exclusion of additional housings and bearings.

Efficiency and noise are affected by radial integration or by introducing a gearbox, but physical experiments are required to quantify these effects. Note that noise as a system property is generally difficult to quantify [96].

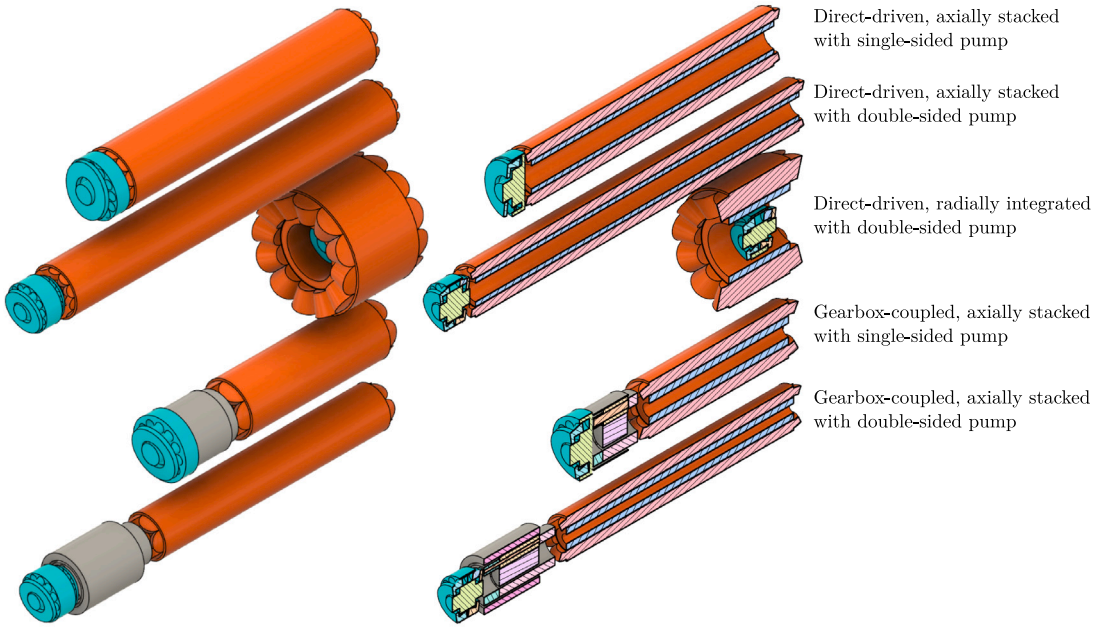

Fig. 22. Visualisation of results for most compact configuration of each concept, see Table 7a.

Manufacturing and cost constraints may reduce the viable design area, e.g., for machines with very low aspect ratios.

7.2. Comparison between direct-driven axially stacked, and radially integrated concept

For a radial integration, double pump hydraulic machines are required due to their longer, thinner design. The double pump type also offers balanced axial forces, enabling reduced bearing size. However, the larger diameter and shorter length of single pumps can result in a more compact configuration for axially stacked components, as the diameter mismatch between the hydraulic and the electric machine is reduced.

The most compact direct-driven, axially stacked setup yields a volume of 5.0 dm^3, and is more compact than the most compact direct-driven, radially integrated design which yields a volume of 6.3 dm^3 (see Table 7a). The reason for this is that to enable radial integration, larger PMSM diameters are required, resulting in increased PMSM volumes. However, the larger PMSM diameters also yield increased PMSM efficiencies for the 12-slot/10-pole machine (see Fig. 8). Larger PMSM diameters lead to increased use of copper material and decreased use of magnet material (see Fig. 12). There is also a significant difference in aspect ratio between the axially stacked and the radially integrated design (see Table 7a). For similar outer diameters or aspect ratios, the radially integrated, direct-driven design is most compact (see Tables 7b and 7c).

Further, there are some considerations for the radially integrated design:

7.2.1. Airgap design

One major decision is whether to flood the "airgap" with oil [23]. If the airgap is not flooded, sealing the airgap requires significant effort, and introduces friction losses due to the sealing elements. Flooding the airgap is sometimes considered for additional cooling (e.g., [40,45]). However, allowing oil in the airgap raises concern over oil degradation and the interaction between the magnets and metallic particles in the oil [97]. Furthermore, as oil has a higher viscosity than air, the airgap length needs to be increased, which requires thicker magnets to maintain electromagnetic performance, and torque losses are increased, especially at cold start [40]. An option for increased cooling without fully flooding the airgap is oil spray cooling [98], which however is typically mainly considered to cool the end windings. Oil spray cooling requires an oil supply (which usually consists of an oil tank, a pump, and a flow control valve) and nozzles to make droplets. The oil is usually delivered back to the tank through gravity or a scavenger pump and needs to be cooled before recirculation. This technology is less attractive for concentrated wound machines which possess a small exposed surface area of the end windings in comparison to distributed wound machines.

7.2.2. Suction performance

Suction performance limits high-speed operation of hydraulic machines [99]. Radially integrated designs complicate the provision of sufficient channel space without bends that create pressure losses.

7.2.3. Churning losses

Hydraulic machines have churning losses caused by piston motion in the oil and by the oil enclosed between the cylinder barrel and the housing [100]. The direct-driven, radially integrated design has no relative speed between the cylinder barrel and the pump "housing". Therefore, the churning losses between barrel and housing are drastically reduced [23]. Churning losses are small at low speeds, but become significant at high speeds [100].

7.2.4. Load support

The double pump design has compensates axial forces but not radial ones [23]. Significant deviations of the rotor from concentric alignment with the stator are amplified by magnetic forces [38]. Therefore, a sufficiently stiff structure is required to guide the radial hydraulic forces [23].

7.3. Comparison between direct-driven and gearbox-coupled concepts

Due to the differing operating speed of the PMSM in gearbox-coupled concepts, a 6-slot/4-pole PMSM was chosen for the gearbox-coupled concepts. For the most compact combinations, the amount of magnetic material used is comparable to the baseline design using a radially integrated 12-slot/10-pole machine, but copper usage is

significantly lower (see Fig. 12). The total mass including the gearbox is in a similar range as the direct-driven concepts (see Figs. 11 and 19). The peak PMSM efficiency for the 6-slot/4-pole machine is similar to the 12-slot/10-pole machine, but note that the gearbox introduces gearing losses (see Table 7) and additional losses (e.g., due to churning, oil splashing, and bearing friction), that have not been quantified in this work.

Nishanth et al. [20] mention some qualitative disadvantages of using gearboxes, such as increased system mass, volume, inertia, and cost. In contrast, this paper does not observe these effects in this generality. Instead, the quantities depend on the specific machine configuration and the aspect ratios considered.

Table 7a shows that using a gearbox can reduce the volume of the active parts to 3.9 dm^3, which is significantly lower than that of the direct-driven concepts. However, these numbers only include active parts, and because adding a gearbox requires additional space for bearings and housings, the relative compactness is overestimated.

The most compact machine combinations are achieved when the electric machine, the hydraulic machine, and the gearbox are axially stacked and have the same outer diameter (see Figs. 20 and 21). That results in machines with very low aspect ratios, e.g., the most compact gearbox-coupled, axially stacked machine has a total length of 736 mm and an outer diameter of 82 mm. For increased aspect ratios, the volume increases due to increased diameter mismatches between the hydraulic machine and the PMSM, and the direct-driven concepts can be more compact.

For the gearbox-driven concepts, a radial integration of the gearbox inside the PMSM is deemed impractical for the considered machines. The gearbox's outer diameter needs to fit inside the PMSM's inner diameter. When limiting the gear width, this results in relatively large airgap diameters and short active lengths for the PMSM. For the considered cooling condition, no PMSM has been identified that offers a sufficiently large airgap diameter to integrate a gearbox, and simultaneously a sufficient active length to maintain thermal equilibrium. Thus, the concepts sketched in Figs. 1(d) and 1(e) would require a higher cooling effort and were discarded in this work.

A typical challenge in gearbox design is noise (see Section 5.5). Noise generally is challenging for each subsystem, and introducing the gearbox as an additional subsystem increases the complexity of the system. Furthermore, introducing the gearbox means additional parts that need maintenance and lubrication. Note that gearboxes typically use different types of oil than hydraulic pumps.

Magnetic gears have been considered as an enabler for increased torque density in electric machines [25,101], but are outside the scope of this paper.

7.4. Efficiency for varying operating conditions

7.4.1. Hydraulic machine efficiency

The overall efficiency of a hydraulic machine is separated into the volumetric efficiency and the hydro-mechanical efficiency. For the pumping case, the volumetric efficiency compares the actual outlet flow to the theoretical outlet flow, and the hydro-mechanical efficiency compares the theoretical drive torque to the actual drive torque. Increasing operating pressures lead to reduced volumetric and increased hydro-mechanic efficiencies. Increasing speed increases both efficiencies at low speeds, but decreases them at high speeds due to incomplete filling and churning losses [102]. Therefore, when sizing a hydraulic machine at a corner operating point, efficiencies well below their peak values must be taken into account.

7.4.2. Electric machine efficiency

The efficiency of PMSM is generally more constant over the operating area than for hydraulic machines. Both iron and copper losses are present in the machine. Copper losses dominate at high current (i.e., high torque), while iron losses dominate at high speeds. The machine designer has some freedom for trade-offs between these losses and can shift the point of peak efficiency to where it is desired [23].

As explained in Section 4.1, increased cooling capacity allows higher losses, and thus enables a more compact design with the consequence of decreased efficiency.

7.4.3. Gearbox efficiency

Planetary gearboxes with one fixed shaft (in this paper, the carrier shaft is fixed, see Section 5.1) possess an efficiency that is almost independent of their load because friction scales proportionally with the load [92].

8. Conclusions

Different types of hydraulic machines suit the different concepts. For the radial integration inside the electric motor, double pump hydraulic machines offer the greatest compactness, whereas the other concepts typically favour a conventional, single pump type due to a reduced diameter mismatch.

The most compact EHEC concept depends on the considered aspect ratio.

For the direct-driven concepts, axial stacking with low airgap diameters results in a good match of the electric machine's outer diameter with the hydraulic machine's outer diameter, but results in electric machine designs with very low aspect ratios. Such low aspect ratios are very unusual, as they pose challenges in both manufacturing and rotor stability. Also, their electromagnetic efficiency is reduced. For balanced aspect ratios with the outer diameter and total length of the machine being similar, the radially integrated concept is most compact.

Gearbox-coupled concepts with radial integration require large inner diameters of the electric machine. Therefore, those designs also require large airgap diameters, which leads to long end windings and short active lengths. End winding losses and limited active length for heat transfer pose cooling challenges. Therefore, of the different gearbox-coupled concepts, only the axially stacked concept is feasible under the considered cooling condition.

Using a gearbox with a ratio of −2.5 lowers the torque requirement on the electric machine by 60%, but when comparing the most compact gearbox-coupled design to the most compact direct-driven design, the volume of the active parts is only reduced by 22%. Considering further parts, such as bearings and housings, is expected to decrease the relative compactness of the gearbox-coupled concept further. The most compact gearbox-coupled concepts have also very low aspect ratios, which is unusual due to challenges for manufacturing and rotor stability. When choosing more balanced aspect ratios, the direct-driven, radially integrated concept is of similar or higher compactness.

An advantage of introducing the gearbox is that the PMSM used requires significantly less copper mass, while the magnet mass and total mass remain comparable to those of the direct-driven, radially integrated design. However, the ratio of magnet mass to copper mass depends on the machine's aspect ratio, i.e., the use of magnet materials can be reduced at the expense of using more copper. Furthermore, adding a gearbox introduces an additional source of losses, and gearboxes are often perceived as noisy, and utilising a gearbox makes the noise behaviour of the overall system more complex.

Based on the results in this paper, the suitability of gearbox-coupled and direct-drive integrated concepts cannot be dismissed without considering further application-specific requirements. However, as the volume reduction of active parts is only 22% for the gearbox-coupled concept in this study, and this neglects bearings and housing, and the benefit is only feasible with an extreme aspect ratio machine, the authors currently do not consider this approach for prototyping. Future experimental plans of the authors include the experimental validation of the direct-driven, radially integrated concept as sketched in Fig. 2.

General abbreviations

Designation	Denotation
BLDC	Brushless Direct Current Machine
DD	Direct-Driven
DP	Double Pump
EHEC	Electro-Hydraulic Energy Converter
FSCW	Fractional-Slot Concentrated Winding
GB	Gearbox
PMSM	Permanent-Magnet Synchronous Machine
SP	Single Pump

General nomenclature

Designation	Denotation	Unit
l_{machine}	Machine's length	m
D_{machine}	Machine's outer diameter	m
OD	Outer diameter	m
V	Volume	m^3

Nomenclature for hydraulics

Designation	Denotation	Unit
n_{hyd}	Rotational speed of the hydraulic machine	rev/s
p	Pressure	Pa
Q_{th}	Theoretical volume flow	m^3/s
T_{th}	Theoretical torque	Nm
V_{hyd}	Hydraulic displacement	m^3/rev
$\varepsilon_{\mathrm{hyd}}$	Setting ratio	–

Nomenclature for electrics

Designation	Denotation	Unit
k_{w}	Winding factor	–
n_{p}	Number of phases	–
n_{pp}	Pole pair count	–
q	Slots per pole per phase	–
z_{c}	Number of turns	–
B	Magnetic flux density	T
B_{rms}	Magnetic loading	T
F	Force	N
I	Current	A
J	Inertia	kg m^2
L_{act}	Active length	m
N_{s}	Slot count	–
Q_{rms}	Electrical loading	A/m
R_{rot}	Rotor radius	m
T	Torque	Nm
σ	Magnetic shear stress	Pa

Indices for planetary gears

Designation	Denotation
0	Sun
1	Planet respectively planet carrier
2	Ring gear
a	Pinion
b	Wheel

Nomenclature for planetary gears

Designation	Denotation	Unit
b	Gear face width	m
b_{carrier}	Planetary carrier width	m
d_{a}	Pinion reference diameter	m
i	Gearbox ratio	–
m	Module	m
m_{n}	Normal module	m
$n_{0,1,2}$	Rotational speed of the sun, carrier shaft, ring gear	rev/s
u	Gear ratio $(z_{\mathrm{b}}/z_{\mathrm{a}}) \geq 1$	–
z	Tooth count	–
F_{t}	Tangential force	N
K_{v}	Dynamic factor	–
K_{A}	Application factor	–
$K_{\mathrm{F},ij}$	Condensed influence factor for tooth bending	–
$K_{\mathrm{H},ij}$	Condensed influence factor for pitting	$\sqrt{\mathrm{N}}/\mathrm{mm}$
$K_{\mathrm{F}\alpha}$	Transverse load factor (root stress)	–
$K_{\mathrm{F}\beta}$	Face load factor (root stress)	–
$K_{\mathrm{H}\alpha}$	Transverse load factor (contact stress)	–
$K_{\mathrm{H}\beta}$	Face load factor (contact stress)	–
K_{γ}	Mesh load factor	–
N_{p}	Number of planets	–
S_{F}	Safety factor for tooth bending	–
S_{H}	Safety factor for pitting	–
T	Torque	Nm
Y_{B}	Rim thickness factor	–
Y_{DT}	Deep tooth factor	–
Y_{F}	Tooth form factor	–
Y_{NT}	Life factor	–
Y_{RrelT}	Relative surface factor	–
Y_{S}	Stress correction factor	–
Y_{ST}	Stress correction factor	–
Y_{X}	Size factor	–
Y_{β}	Helix angle factor	–
$Y_{\delta\mathrm{relT}}$	Relative notch sensitivity factor	–
Y_{S}	Stress correction factor	–
Y_{ST}	Stress correction factor	–
Y_{X}	Size factor	–
Y_{β}	Helix angle factor	–
$Y_{\delta\mathrm{relT}}$	Relative notch sensitivity factor	–
$Z_{\mathrm{B,D}}$	Tooth contact factor	–
Z_{E}	Elasticity coefficient	$(\mathrm{N/mm^2})^{0.5}$
Z_{H}	Zone factor	–
Z_{L}	Lubricant factor	–
Z_{NT}	Life factor	–
Z_{R}	Roughness factor	–
Z_{V}	Velocity factor	–
Z_{W}	Work hardening factor	–
Z_{X}	Size factor	–
Z_{β}	Helix angle factor (pitting)	–
Z_{ε}	Contact ratio factor (pitting)	–
ε_{α}	Number of contacting teeth for spur gear	–
ε_{β}	Number of additional teeth in contact due to helix angle	–
ε_{γ}	Number of contacting teeth	–
η	Efficiency	–
σ_{F}	Tooth root stress	Pa
σ_{F0}	Nominal tooth root stress	Pa

Designation	Denotation	Unit
σ_{Flim}	Nominal stress number (bending)	Pa
σ_{FG}	Tooth root stress limit	Pa
σ_{FP}	Permissible bending stress	Pa
σ_H	Contact stress	Pa
σ_{H0}	Nominal contact stress in the pitch point	Pa
σ_{Hlim}	Allowable stress number (contact)	Pa
σ_{HG}	Pitting stress limit	Pa
σ_{HP}	Permissible contact stress	Pa

CRediT authorship contribution statement

Thomas Heeger: Writing – review & editing, Writing – original draft, Visualization, Methodology, Formal analysis, Conceptualization. **Martin West:** Writing – review & editing, Methodology, Conceptualization. **Liselott Ericson:** Writing – review & editing, Supervision, Project administration, Funding acquisition.

Declaration of Generative AI and AI-assisted technologies in the writing process

During the preparation of this work the authors used ChatGPT in order to assist in writing code for the visualisation of the results. The tool/service was not used to develop the sizing method or equations. After using this tool/service, the authors reviewed and edited the content as needed and take full responsibility for the content of the published article.

Funding

This research was funded by the Swedish Electromobility Centre (SEC) with grant number 13070 and the Swedish Energy Agency (Energimyndigheten) with grant number P2023-00594.

Declaration of competing interest

The authors declare that they have no known competing financial interests or personal relationships that could have appeared to influence the work reported in this paper.

Acknowledgement

The authors would like to thank GWJ Technology GmbH for providing their software for gear calculation.

Data availability

No data was used for the research described in the article.

References

[1] Kärnell S. On electrified fluid power systems in mobile machinery (Ph.D. thesis), Linköping University; 2022, URL https://www.diva-portal.org/smash/record.jsf?pid=diva2:1688737&dswid=8813.

[2] Love LJ, Lanke E, Alles P. Estimating the impact (energy, emissions and economics) of the US fluid power industry. (December). Oak Ridge, USA: Oak Ridge National Laboratory; 2012, URL http://www.osti.gov/servlets/purl/1061537/.

[3] Lynch LA, Zigler BT. Estimating energy consumption of mobile fluid power in the United States. Tech. rep. November, National Renewable Energy Laboratory; 2017.

[4] Grote K-H, Bender B, Göhlich D, editors. Dubbel - Taschenbuch für den Maschinenbau. 25. Auflag. Berlin, Heidelberg: Springer Berlin Heidelberg; 2018, http://dx.doi.org/10.1007/978-3-662-54805-9, URL http://link.springer.com/10.1007/978-3-662-54805-9.

[5] Padovani D, Dimitriou P, Minav T. Challenges and solutions for designing Energy-Efficient and Low-Pollutant Machines in Off-Road hydraulics. Energy Convers Manag: X 2024;21(December 2023):100526. http://dx.doi.org/10.1016/j.ecmx.2024.100526, URL https://doi.org/10.1016/j.ecmx.2024.100526.

[6] Hagen D, Padovani D, Choux M. A comparison study of a novel self-contained electro-hydraulic cylinder versus a conventional valve-controlled actuator—Part 2: Energy efficiency. Actuators 2019;8(4). http://dx.doi.org/10.3390/ACT8040078.

[7] Qu S, Zappaterra F, Vacca A, Busquets E. An electrified boom actuation system with energy regeneration capability driven by a novel electro-hydraulic unit. Energy Convers Manage 2023;293(May):117443. http://dx.doi.org/10.1016/j.enconman.2023.117443.

[8] Hao Y, Quan L, Qiao S, Ge L, Li Z, Zhao B. Energy and operation characteristics of electric excavator with innovative hydraulic-electric dual power drive boom system. IEEE Access 2023;11(September):107265–75. http://dx.doi.org/10.1109/ACCESS.2023.3314338.

[9] Parker Hannifin Corporation. Configured ePumps: Electro-hydraulic pumps (EHPs) for construction, truck, mining, material handling, agriculture and forestry applications. 2023, URL https://www.parker.com/content/dam/Parker-com/Literature/Hydraulic-Pump-Division/Parker_HPS_192-300122_ePump_catalog_NA.pdf. [Accessed 7 August 2024].

[10] Bosch Rexroth AG. eLION Motor EMS1. Heavy duty design for Off-Highway applications. RE98771/2024-08-19. 2024.

[11] Albrecht H, Rehbein M, Weisshaupt E, Wiest W. Electrohydraulic drive system. 2024, Patent Application WO2024008432A1.

[12] Jones JL. Combination electric motor and compressor. United States Patent Office; 1929, Patent US1926444A.

[13] Voith Turbo GmbH & CoKG. Motor / pump hybrid system EPAI for high and medium-pressure applications. 2012, URL http://www.hypower.com.hk/pdf/Voith_Turbo/890_e_g1891_en.pdf. [Accessed 17 June 25].

[14] Döhla W, Bauer J, Kemnitz R. Integrated smart hydraulic displacement machine for closed systems. In: 12th international fluid power conference, 12. IFK. Technische Universität Dresden; 2020, p. 121–7. http://dx.doi.org/10.25368/2020.101, URL https://nbn-resolving.org/urn:nbn:de:bsz:14-qucosa2-712258.

[15] Heeger T. Design of electro-hydraulic energy converters : With focus on integrated designs and valve plate rotation. In: Linköping studies in science and technology. Licentiate thesis, vol. 1971, Linköping: Linköping University Electronic Press; 2023, http://dx.doi.org/10.3384/9789180752442, URL https://urn.kb.se/resolve?urn=urn:nbn:se:liu:diva-194262.

[16] Pietrzyk T, Roth D, Schmitz K, Jacobs G. Design study of a high speed power unit for electro hydraulic actuators (EHA) in mobile applications. In: 11th international fluid power conference, 11. IFK, 19–21 March, 2018, Aachen, Germany. 2018, p. 232—245. http://dx.doi.org/10.18154/RWTH-2018-224632.

[17] Zhang H, Kalidindi SKR, Huard S, Chu Y-S, Natarajan S, Burgess B, et al. Electric motor with integrated hydraulic pump and motor controller. 2023, Patent US11788529B2.

[18] Lindh P, Di C, Laurila L, Scherman E, Handroos H, Pyrhönen J. Compact electrohydraulic energy converter for off-road machines. In: 2021 IEEE international electric machines & drives conference. IEMDC, IEEE; 2021, p. 1–5. http://dx.doi.org/10.1109/IEMDC47953.2021.9449590.

[19] Vickers. Integrated Motor Pump. 2023, URL https://www.eaton.com/ecm/groups/public/@pub/@eaton/@hyd/documents/content/pll_1413.pdf. [Accessed 11 April 2023].

[20] Nishanth FNU, Bohach G, Nahin MM, de Ven JV, Severson EL. Development of an integrated electro-hydraulic machine to electrify off-highway vehicles. IEEE Trans Ind Appl 2022;58(5):6163–74. http://dx.doi.org/10.1109/tia.2022.3189609.

[21] Zhu D, Fu Y, Han X, Li Z. Design and experimental verification on characteristics of electro-hydraulic pump. Mech Syst Signal Process 2020;144. http://dx.doi.org/10.1016/j.ymssp.2020.106771, URL https://doi.org/10.1016/j.ymssp.2020.106771.

[22] Jacobs G, Schmitz K, Pietrzyk T, Roth D. Schlussbericht zu IGF-Vorhaben Nr. 19224N: Dezentrale kompakte Hydraulikversorgung durch High-Speed-Komponenten. 2020.

[23] Heeger T, West M, Heybroek K, Ericson L. Methodology for dimensioning of integrated electro-hydraulic machines. In: Proceedings of the 18:th Scandinavian international conference on fluid power, SICFP23, 30 May - 1 June, 2023, Tampere, Finland. 2023, URL https://liu.diva-portal.org/smash/record.jsf?pid=diva2:1820972&dswid=-8547.

[24] Moog. Electrohydrostatic pump unit. 2022, URL https://www.moog.co.in/content/dam/sites/moog/products/electrohydrostatic-pump-unit/Moog-EPU-Catalog-en.pdf. [Accessed 25 May 2023].

[25] Nishanth F, Ven JVD, Severson EL. Evaluation of torque-dense electric machine technology for off-highway vehicle electrification. IEEE Trans Ind Appl 2024;60(2):3062–74. http://dx.doi.org/10.1109/TIA.2023.3335890.

[26] Handle W, Helbig A. Motor cooling via hydraulic fluid. 2023, Patent US11773882B2.

[27] Busquets E, Neumann U, Vacca A, Zappaterra F. Electric and hydraulic machine. 2024, Patent US11990819B2.

[28] Zhang H, Kalidindi SKR, Huard SR. Systems and assemblies for an electric motor with integrated hydraulic pump and electronic drive device. 2023, Patent Application US2023383748A1.

[29] Zhang H, Kalidindi SKR, Gangadharan N, Wegmann B, Huard SR. Integrated assembly of an electric motor, hydraulic pump, and electronic drive device and associated cooling configuration. 2025, Patent US12398738B2.

[30] Vacca A, Assaf H, Zhang H, Zappaterra F. Integrated electrohydraulic actuator. 2024, Patent Application WO2024205693A1.

[31] Sarode S, Shang L, Vacca A, Sudhoff S. Flux weakening operation based design of an integrated electrohydraulic axial piston unit. In: Proceedings of BATH/ASME 2022 symposium on fluid power and motion control. 2022, http://dx.doi.org/10.1115/FPMC2022-89718.

[32] Sarode S, Assaf H, Shang L, Vacca A, Sudhoff S. Optimizing Electric Machines for Off-Road Mobile Applications. In: Proceedings of the 18:th scandinavian international conference on fluid power, SICFP23, 30 May - 1 June, 2023, tampere, Finland. 2023.

[33] Assaf H, Sarode S, Vacca A, Sudhoff SD. Electric machine sizing consideration for ePumps in mobile hydraulics. Energy Sci Eng 2024;12(3):793–809. http://dx.doi.org/10.1002/ese3.1654, URL https://onlinelibrary.wiley.com/doi/10.1002/ese3.1654.

[34] Fu YL, Li ZF, Zhang P, Chen HM. Mechanical and hydraulic joint modeling and simulation about elec-pump. Adv Mater Res 2013;694 697:614–20. http://dx.doi.org/10.4028/www.scientific.net/AMR.694-697.614.

[35] Zhu D, Fu Y, Fu J, Yu L. Power losses and thermal analysis of a designed electro-hydraulic pump. In: 2017 IEEE international conference on mechatronics and automation, ICMA 2017, 6–9 August, Takamatsu, Japan. 2017, p. 728–33. http://dx.doi.org/10.1109/ICMA.2017.8015906.

[36] Zhu D, Wang M, Fu Y. Design and validation of electro-hydraulic pumping unit for smart manufacturing. Int J Adv Manuf Technol 2022. http://dx.doi.org/10.1007/s00170-022-09148-6, URL https://doi.org/10.1007/s00170-022-09148-6.

[37] Wang T, Wang Q. Coupling effects of a novel integrated electro-hydraulic energy conversion unit. Int J Appl Electromagn Mech 2015;47(1):153–62. http://dx.doi.org/10.3233/JAE-140004.

[38] Wang T, Wang H, Zhou Z. Unbalanced magnetic torque in electrohydraulic energy conversion unit considering rotor axis deflection. IEEE Trans Magn 2016;52(6). http://dx.doi.org/10.1109/TMAG.2016.2528894.

[39] Wang T, Zhou Z. A compact hydrostatic-driven electric generator: Design, prototype, and experiment. IEEE/ASME Trans Mechatronics 2016;21(3):1612–9. http://dx.doi.org/10.1109/TMECH.2015.2504491.

[40] Powell DJ. Modelling of high power density electrical machines for aerospace (Ph.D. thesis), University of Sheffield; 2003.

[41] Wang J, Zhang T, Zhang H, Zhang Z, Chen H. Design optimization of electrical structure parameters of induction asynchronous mechanical–electric–hydraulic power coupler. Processes 2023;11(7):2217. http://dx.doi.org/10.3390/pr11072217, URL https://www.mdpi.com/2227-9717/11/7/2217.

[42] Liu B, Zhang T, Zhang H, Zhen Z, Cao Y. Simulation analysis on electromagnetic vibration and noise of novel mechatronic-electro-hydraulic coupler. Machines 2022;(10):762. http://dx.doi.org/10.3390/machines10090762.

[43] Zhang L, Zhang H, Liu B, Zhang Z, Jiang Y. Investigation on the external characteristics of permanent magnet synchronous mechatronic-electro-hydraulic coupler. Adv Mech Eng 2024;16(5):1–20. http://dx.doi.org/10.1177/16878132241253667, URL https://journals.sagepub.com/doi/10.1177/16878132241253667.

[44] Jiang Y, Zhang H, Qiu L, Li M, Zhang L. Engineering analysis with boundary elements research on energy loss of mechatronic electro-hydraulic coupler using radial basis function collocation method. Eng Anal Bound Elem 2025;176(December 2024):106231. http://dx.doi.org/10.1016/j.enganabound.2025.106231, URL https://doi.org/10.1016/j.enganabound.2025.106231.

[45] Ponomarev P, Polikarpova M, Heinikainen O, Pyrhönen J. Design of integrated electro-hydraulic power unit for hybrid mobile working machines. In: Proceedings of the 2011 14th European conference on power electronics and applications, EPE 2011, 30 August - 1 September 2011, Birmingham, United Kingdom. 2011.

[46] Åman R, Handroos H, Ponomarev P, Pyrhönen J. Electro-hydraulic hybrid actuator system using integrated power unit. In: 8th international fluid power conference, IFK2012, 26–28 March, 2012, Dresden, Germany. 2012, URL http://gfpsweb.org/sites/default/files/external_pages/IFK_2012/Welcome.html.

[47] Ponomarev P, Åman R, Handroos H, Immonen P, Pyrhönen J, Laurila L. High power density integrated electro-hydraulic energy converter for heavy hybrid off-highway working vehicles. IET Electr Syst Transp 2014;4(4):114–21. http://dx.doi.org/10.1049/iet-est.2013.0009.

[48] Ponomarev P, Minav T, Åman R, Luostarinen L. Integrated electro-hydraulic machine with self-cooling possibilities for non-road mobile machinery. Stroj Vestnik/J Mech Eng 2015;61(3):207–13. http://dx.doi.org/10.5545/sv-jme.2014.2017.

[49] Ponomarev P. Tooth-coil permanent magnet synchronous machine design for special applications (Ph.D. thesis), Lappeenranta University of Technology; 2013.

[50] Nishanth F, Bohach G, Nahin MM, Van de Ven J, Severson EL. Design of an axial flux machine with an integrated hydraulic pump for off-highway vehicle electrification. In: 2020 IEEE energy conversion congress and exposition. IEEE; 2020, p. 1772–9. http://dx.doi.org/10.1109/ECCE44975.2020.9235731, URL https://ieeexplore.ieee.org/document/9235731/.

[51] Nahin MM, Bohach GR, Nishanth FN, Severson EL, Van De Ven JD. Dynamic modeling and design of a radial hydrostatic piston pump for integrated pump-motor. In: Proceedings of ASME/BATH 2021 symposium on fluid power and motion control, FPMC 2021, October 19–21, 2021, Online. 2021, http://dx.doi.org/10.1115/FPMC2021-68788.

[52] Nahin MM. Design of a high-speed radial hydrostatic piston pump for integration with an electric motor (Ph.D. thesis), University of Minnesota; 2024.

[53] Matias L, Plummer A, Johnston N. Experimental and analytical investigation of a highly integrated electro-hydraulic pump motor unit. In: The 19th Scandinavian international conference on fluid power, SICFP'25, June 2–4, 2025, Linköping, Sweden. 2025.

[54] Zappaterra F, Vacca A, Sudhoff SD. A compact design for an electric driven hydraulic gear machine capable of multiple quadrant operation. Mech Mach Theory 2022;177:105024. http://dx.doi.org/10.1016/j.mechmachtheory.2022.105024.

[55] Qu S, Zappaterra F, Vacca A, Liu Z, Busquets E. Experimental verification of an electro-hydraulic actuation system driven by an integrated electro-hydraulic unit. Int J Fluid Power 2023;24:327–60. http://dx.doi.org/10.13052/ijfp1439-9776.2427.

[56] Wustmann W, Helduser S, Schuffenhauer U, Kuss H, Michalke N. Fully integrated electric-hydrostatic drive based on a gear pump and a switched reluctance motor. In: The tenth Scandinavian international conference on fluid power, SICFP'07, 21–23 May, 2007, Tampere, Finland. 2007, p. 327–39, URL https://www.tib.eu/en/search/id/tema%3ATEMA20090801910/Fully-integrated-electric-hydrostatic-drive-based/.

[57] Zappaterra F, Pan D, Ransegnola T, Vacca A, Sudhoff SD, Busquets E. A novel electro-hydraulic unit design based on a shaftless integration of an internal gear machine and a permanent magnet electric machine. Energy Convers Manage 2024;310(April):118432. http://dx.doi.org/10.1016/j.enconman.2024.118432, URL https://doi.org/10.1016/j.enconman.2024.118432.

[58] Fiebig W, Ignacy D, Marek C, Hubert K. A vane pump integrated with an electric motor. In: The 9th international fluid power conference, 9. IFK, 24–26 March, 2014, Aachen, Germany. 2014.

[59] Fiebig W, Cependa P, Jedraszczyk P, Kuczwara H. Innovative solution of an integrated motor pump assembly. In: ASME/bATH 2017 symposium on fluid power and motion control, FPMC 2017, 16–19 October, 2017, Sarasota, Florida, USA. 2017, http://dx.doi.org/10.1115/FPMC2017-4277.

[60] Ciurys MP, Fiebig W. Experimental investigation of a double-acting vane pump with integrated electric drive. Energies 2021;14:5949. http://dx.doi.org/10.3390/en14185949.

[61] Gamez-Montero P, Castilla R, Codina E, Freire J, Morató J, Sanchez-Casas E, et al. GeroMAG: In-house prototype of an innovative sealed, compact and non-shaft-driven gerotor pump with magnetically-driving outer rotor. Energies 2017;10(4):435. http://dx.doi.org/10.3390/en10040435, URL http://www.mdpi.com/1996-1073/10/4/435.

[62] Leati E, Poltschak F, Scheidl R. An electromagnetically actuated high frequency oscillation pump. Mechatronics 2017;47:233–45. http://dx.doi.org/10.1016/j.mechatronics.2016.10.009, URL https://doi.org/10.1016/j.mechatronics.2016.10.009.

[63] Khamitov A, Swanson J, Van De Ven J, Severson EL. Modeling, design, and testing of a linear electric-hydraulic conversion machine for electrification of off-highway vehicles. IEEE Trans Ind Appl 2021;57(3):2449–59. http://dx.doi.org/10.1109/TIA.2021.3066084.

[64] Pietrzyk T. Innenzahnradpumpe für die Elektrifizierung mobiler Anwendungen am Beispiel einer autarken dezentralen elektro-hydraulischen achse (Ph.D. thesis), RWTH Aachen University; 2022.

[65] Lindh P, Tiainen J, Grönman A, Turunen-saaresti T, Di C, Laurila L, et al. Two cooling approaches of an electrohydraulic energy converter for non-road mobile machinery. IEEE Trans Ind Appl 2023;59(2):736–44. http://dx.doi.org/10.1109/TIA.2022.3207983.

[66] Ivantysyn J, Ivantysynova M. Hydrostatic pumps and motors: principles, design, performance, modelling, analysis, control, and testing. New Delhi: Akademia Books International; 2001.

[67] Achten PAJ. Power density of the floating cup axial piston principle. In: Proceedings of the ASME 2004 international mechanical engineering congress and expo (IMECE2004), November 13–19, 2004, Anaheim, California, USA. ASME; 2004, p. IMECE2004–59006. http://dx.doi.org/10.1115/imece2004-59006.

[68] Manring ND, Mehta VS, Nelson BE, Graf KJ, Kuehn JL. Scaling the speed limitations for axial-piston swash-plate type hydrostatic machines. J Dyn Syst Meas Control Trans ASME 2014;136(3). http://dx.doi.org/10.1115/1.4026129.

[69] Ericson L, Forssell J. A novel axial piston pump/motor principle with floating pistons: Design and testing. In: BATH/aSME 2018 symposium on fluid power and motion control (FPMC2018), September 12–14, 2018, Bath, United kingdom. American Society of Mechanical Engineers; 2018, p. FPMC2018–8937. http://dx.doi.org/10.1115/fpmc2018-8937.

[70] Lee W, Li S, Han D, Sarlioglu B, Minav TA, Pietola M. A review of integrated motor drive and wide-bandgap power electronics for hydrostatic actuators. IEEE Trans Transp Electrification 2018;4(3):684–93. http://dx.doi.org/10.1109/TTE.2018.2853994.
[71] European Commission. Annexes to the proposal for a regulation of the European Parliament and of the Council establishing a framework for ensuring a secure and sustainable supply of critical raw materials and amending regulations (EU) 168/2013, (EU) 2018/858, 2018/1724 and (EU). 2023.
[72] Krings A, Monissen C. Review and trends in electric traction motors for battery electric and hybrid vehicles. In: Proceedings - 2020 international conference on electrical machines, ICEM 2020. 2020, p. 1807–13. http://dx.doi.org/10.1109/ICEM49940.2020.9270946.
[73] da Silva MD. Design and optimization of spoke type permanent magnet synchronous machines. A rare-earth element free solution for electromobility (Ph.D. thesis), Uppsala University; 2025, URL https://uu.diva-portal.org/smash/get/diva2:1950231/FULLTEXT01.pdf.
[74] Yang R, Schofield N, Emadi A. Comparative study between interior and surface permanent magnet traction machine designs. In: 2016 IEEE transportation electrification conference and expo (ITEC), Dearborn, MI, USA. 2016, p. 1–6. http://dx.doi.org/10.1109/ITEC.2016.7520249.
[75] Lipo TA. Introduction to AC machine design. New Jersey: Wiley & Sons, Limited, John, Hoboken; 2017.
[76] Lefevre Y, El-Aabid S, Llibre J-F, Henaux C, Touhami S. Performance assessment tool based on loadability concepts. Int J Appl Electromagn Mech 2019;59(2):687–94. http://dx.doi.org/10.3233/jae-171059.
[77] Krishnan R. Permanent magnet synchronous and brushless DC motor drives. Boca Raton, USA: Taylor & Francis; 2010.
[78] Staton D. Improving motor efficiency and motor miniaturisation the role of thermal simulation (Tutorial 3 at international conference on electrical machines (ICEM2012), 2–5 September 2012, Marseille, France). 2012, URL https://www.scribd.com/document/451214696/Dave-Staton-Thermal-Design-pdf.
[79] Jacobs G. Maschinengestaltung, Vorlesungsumdruck für das Wintersemester. Aachen: Druck & Verlagshaus Mainz; 2014.
[80] Tawarawala P, Sarode S, Assaf H, Vacca A, Shang L, Sudhoff SD. A study on design methodologies for compact electric machines used in electrified mobile hydraulics. Int J Fluid Power 2024;25(3):375–412. http://dx.doi.org/10.13052/ijfp1439-9776.2534.
[81] Wang J, Xia ZP, Howe D. Three-phase modular permanent magnet brushless machine for torque boosting on a downsized ICE vehicle. IEEE Trans Veh Technol 2005;54(3):809–16. http://dx.doi.org/10.1109/TVT.2005.847224.
[82] Libert F, Soulard J. Investigation on pole-slot combinations for permanent-magnet machines with concentrated windings. 2004, URL https://www.researchgate.net/publication/237458473_Investigation_on_Pole-Slot_Combinations_for_Permanent-Magnet_Machines_with_Concentrated_Windings. [Accessed 5 September 2025].
[83] Ansys Inc. Ansys motor-CAD. Electric machine design software. 2025, URL https://www.ansys.com/products/electronics/ansys-motor-cad. [Accessed 17 August 2025].
[84] International Organization for Standardization. ISO 6336-1: Calculation of load capacity of spur and helical gears — Part 1: Basic principles, introduction and general influence factors. 2019.
[85] International Organization for Standardization. ISO 6336-2: Calculation of Load Capacity of Spur and Helical Gears — Part 2: Calculation of surface durability (pitting). 2019.
[86] International Organization for Standardization. ISO 6336-3: Calculation of load capacity of spur and helical gears — Part 3: Calculation of tooth bending strength. 2019.
[87] International Organization for Standardization. ISO TS 6336-20: Calculation of load capacity of spur and helical gears — Part 20: Calculation of scuffing load capacity — Flash temperature method. 2022.
[88] International Organization for Standardization. ISO TS 6336-21: Calculation of spur and helical gears — Part 21: Calculation of scuffing load capacity — Integral temperature method. 2022, 2022.
[89] GWJ Technology GmbH. GWJ eAssistant: Planetary gear trains according to DIN 3960, DIN 3990, ISO 6336 and further standards. URL https://www.eassistant.eu/en/eassistant/gear-calculation/planetary-gear-trains.html. [19 August 2024].
[90] International Organization for Standardization. ISO TR 13989-1: Calculation of scuffing load capacity of cylindrical, bevel and hypoid gears - Part 1: Flash temperature method. 2000.
[91] for Standardization IO. ISO TR 13989-2: Calculation of scuffing load capacity of cylindrical, bevel and hypoid gears - Part 2: Integral temperature method. 2000.
[92] Jacobs G. Maschinengestaltung, Vorlesungsumdruck für das Sommersemester. Aachen: Druck & Verlagshaus Mainz; 2015.
[93] American Gear Manufacturers Association. American national standard ANSI/AGMA 6123-c16. Design manual for enclosed epicyclic gear drives. In: Design. 2016.
[94] Hao D, Wang D. Finite-element modeling of the failure of interference-fit planet carrier and shaft assembly. Eng Fail Anal 2013;33:184–96. http://dx.doi.org/10.1016/j.engfailanal.2013.04.029.
[95] Roth D, Jacobs G, Kramer A, Krech M, Pietrzyk T, Schmitz K. Bauraumreduktion durch Drehzahlanhebung – Einsatz von High-Speed-Antrieben in elektrohydraulischen Linearaktuatoren für mobile Anwendungen. In: 7. Fachtagung, hybride und energieeffiziente Antriebe für mobile Arbeitsmaschinen, 20. February 2019, Karlsruhe, Germany, 2019, p. 73–93.
[96] Gieras JF, Wang C, Lai JC. Noise of polyphase electric motors. CRC Press; 2018, http://dx.doi.org/10.1201/9781420027730, URL https://www.taylorfrancis.com/books/9781420027730.
[97] Fassbender D, Zakharov V, Minav T. Utilization of electric prime movers in hydraulic heavy-duty-mobile-machine implement systems. Autom Constr 2021;132. http://dx.doi.org/10.1016/j.autcon.2021.103964, URL https://doi.org/10.1016/j.autcon.2021.103964.
[98] Shams Ghahfarokhi P, Podgornovs A, Kallaste A, Marques Cardoso AJ, Belahcen A, Vaimann T. The oil spray cooling system of automotive traction motors: The state of the art. IEEE Trans Transp Electrification 2023;9(1):428–51. http://dx.doi.org/10.1109/TTE.2022.3189596.
[99] Manring ND. Fluid power pumps and motors: Analysis, design and control. McGraw Hill Book CO; 2013.
[100] Zhang J, Li Y, Xu B, Pan M, Lv F. Experimental study on the influence of the rotating cylinder block and pistons on churning losses in axial piston pumps. Energies 2017;10(5):662. http://dx.doi.org/10.3390/en10050662.
[101] Zhu ZQ, Li HY, Deodhar R, Pride A, Sasaki T. Recent developments and comparative study of magnetically geared machines. CES Trans Electr Mach Syst 2020;2(1):13–22. http://dx.doi.org/10.23919/tems.2018.8326448.
[102] Vacca A, Franzoni G. Hydraulic fluid power: Fundamentals, Applications, and Circuit Design. John Wileys and Sons; 2021.